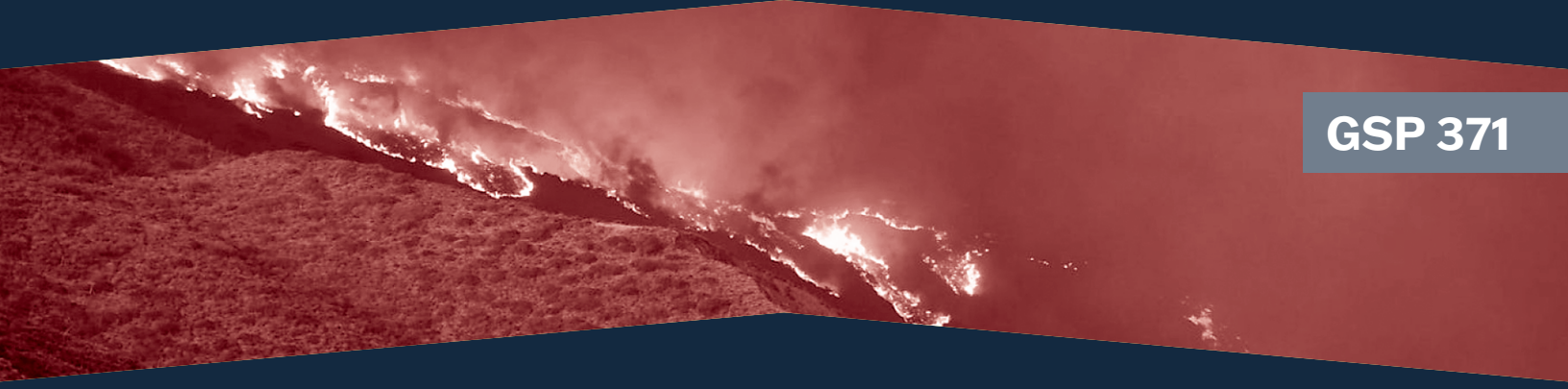


GSP 371

# Geo-Extreme 2025



## Civil Infrastructure, Geomaterials, and Case Histories



Selected Papers from Geo-Extreme 2025
Long Beach, California • November 2–5, 2025


EDITED BY

Christopher L. Meehan, Ph.D., P.E., BC.GE;
James A. McKelvey III, Ph.D., P.E., BC.GE;
Adda Athanasopoulos-Zekkos, Ph.D.;
Miguel A. Pando, Ph.D., P.Eng.; Nina Stark, Ph.D.;
and Ming Xiao, Ph.D., P.E., BC.GE



ASCE

G-I GEO-INSTITUTE

GEOTECHNICAL SPECIAL PUBLICATION NO. 371

# GEO-EXTREME 2025

## *CIVIL INFRASTRUCTURE, GEOMATERIALS, AND CASE HISTORIES*

SELECTED PAPERS FROM GEO-EXTREME 2025

November 2–5, 2025
Long Beach, California

SPONSORED BY

The Geo-Institute
of the American Society of Civil Engineers

EDITED BY
Christopher L. Meehan, Ph.D., P.E., BC.GE
James A. McKelvey III, Ph.D., P.E., BC.GE
Adda Athanasopoulos-Zekkos, Ph.D.
Miguel A. Pando, Ph.D., P.Eng.
Nina Stark, Ph.D.
Ming Xiao, Ph.D., P.E., BC.GE

**Published by the American Society of Civil Engineers**

Published by American Society of Civil Engineers
1801 Alexander Bell Drive
Reston, Virginia, 20191-4382
www.asce.org/publications | ascelibrary.org

Any statements expressed in these materials are those of the individual authors and do not necessarily represent the views of ASCE, which takes no responsibility for any statement made herein. No reference made in this publication to any specific method, product, process, or service constitutes or implies an endorsement, recommendation, or warranty thereof by ASCE. The materials are for general information only and do not represent a standard of ASCE, nor are they intended as a reference in purchase specifications, contracts, regulations, statutes, or any other legal document. ASCE makes no representation or warranty of any kind, whether express or implied, concerning the accuracy, completeness, suitability, or utility of any information, apparatus, product, or process discussed in this publication, and assumes no liability therefor. The information contained in these materials should not be used without first securing competent advice with respect to its suitability for any general or specific application. Anyone utilizing such information assumes all liability arising from such use, including but not limited to infringement of any patent or patents.

ASCE and American Society of Civil Engineers—Registered in U.S. Patent and Trademark Office.

*Photocopies and permissions.* Permission to photocopy or reproduce material from ASCE publications can be requested by sending an e-mail to permissions@asce.org or by locating a title in ASCE's Civil Engineering Database (http://cedb.asce.org) or ASCE Library (http://ascelibrary.org) and using the "Permissions" link.

***Errata:*** **Errata, if any, can be found at https://doi.org/10.1061/9780784486511**

Copyright © 2025 by the American Society of Civil Engineers.
All Rights Reserved.
ISBN 978-0-7844-8651-1 (PDF)
Manufactured in the United States of America.

# Preface

The Embankments, Dams, and Slopes (EDS) Technical Committee of the ASCE Geo-Institute organized a timely and interesting specialty conference in 2021 in Savannah, Georgia, entitled *Geo-Extreme 2021: Geotechnical Engineering for Extreme Events*. This 2021 conference was intended as an inaugural specialty conference, and the beginning of a series of planned conferences organized by the EDS committee seeking to address the many societal challenges that are posed by extreme events such as: earthquakes, hurricanes, landslides, debris flows, wildfires, tornadoes, extreme rainfall events, blizzards, and other extreme loading events caused by changing weather patterns. This 2021 conference built on three previous slope stability related conferences that were organized by the EDS committee, two in 1966 and 1992 at the University of California at Berkeley and one in 2013 in San Diego. Strong impetus for that meeting was provided by a number of very significant extreme events in the United States, starting with Hurricanes Katrina in 2005 and Sandy in 2012 followed by Hurricanes Harvey, Irma, and Maria in 2017, and then Hurricanes Laura, Delta, and Zeta in 2020, which all caused widespread damage to communities at large, and particular damage to natural slopes and engineered structures that are the purview of the EDS Committee.

Since the 2021 conference, the onslaught of extreme loading events in the United States has continued unabated, with significant loss of life and severe financial consequences to communities that are unprecedented. The impact of major hurricanes including Ian, Ida, Idalia, Helene, and Milton has been strongly felt in coastal communities but also ranging far inland. Extreme rainfall and flood events have caused damages averaging in excess of a billion dollars annually, particularly in California. Severe storms, winds, and flooding also battered Kentucky heavily in 2025. Wildfires brought significant destruction and caused numerous deaths in Hawaii's Lahaina fire of 2023, the Smokehouse Creek fire in Texas and Oklahoma in 2024, and in California with the Park Fire in 2024 and wildfires in Southern California in 2025. The 2023 fire season was also particularly significant in Canada, which saw 45,700,000 acres of land burn across ten provinces and three territories.

Following these extreme events, the EDS Committee has proposed and organized the current specialty conference, *Geo-Extreme 2025: Geotechnical Engineering for Extreme Events*. The goal of this conference is to continue to draw attention to the pressing problems posed by extreme events, and to identify the critical role that geotechnical engineers and the civil engineering profession as a whole can play in mitigating the effects of these events, both before they occur, as well as after – that is, "building back safer" in a way that benefits both the built and natural environments.

Historical records show that the number of billion-dollar extreme events are on the rise. Mitigating the consequences of future extreme events requires geo-professionals taking timely actions, including evaluation of existing earthen structures, design and construction of protective structures in areas where an increased probability of damage is expected, refinement of existing geotechnical designs, and development of new adaptive measures and risk assessment tools. To achieve these objectives, the Geo-Extreme 2025 conference will comprise a multi-disciplinary forum between geotechnical engineers and other professionals from related disciplines, such as scientists, various

© ASCE

types of engineers, emergency managers, resilience and sustainability investigators, insurance experts, and policy makers, to provide solutions that properly cope with and address the wide variety of extreme events that can occur.

There are five volumes containing the full collection of papers presented at Geo-Extreme 2025: Geotechnical Engineering for Extreme Events, which was held on November 2-5, 2025, in Long Beach, California. These five volumes are subtitled: (1) Remote Sensing, Instrumentation, Big Data, and Decision Making, (2) Geotechnical Earthquake Engineering, (3) Civil Infrastructure, Geomaterials, and Case Histories, (4) Different Climates and the Coastal Zone, and (5) Permafrost, Wildfires, and Other Emerging Challenges in Geotechnical Engineering, respectively. These five volumes include over 130 contributions that span 25 subtopic areas of the conference, as noted in the subsequent tables of contents for each volume. Each of the five volumes are Geotechnical Special Publications (GSPs), containing papers that were reviewed in accordance with ASCE GSP standards. Each paper was subjected to technical review by two or more independent peer reviewers, and publication required concurrence by at least two peer reviewers.

The Editors gratefully acknowledge the immeasurable contributions of the countless individuals who made Geo-Extreme 2025 and these published proceedings possible, especially the reviewers, session chairs, organizing committee members, and ASCE staff listed in the acknowledgements.

The Proceedings Editors,

Christopher L. Meehan, Ph.D., P.E., BC.GE, F.ASCE, University of Delaware
James A. McKelvey, III, Ph.D., P.E., BC.GE, F.ASCE, Earth Engineering Incorporated
Adda Athanasopoulos-Zekkos, Ph.D., M.ASCE, University of California, Berkeley
Miguel A. Pando, Ph.D., P.Eng., M.ASCE, Drexel University
Nina Stark, Ph.D., M.ASCE, University of Florida
Ming Xiao, Ph.D., P.E., BC.GE, F.ASCE, Pennsylvania State University

© ASCE

# Acknowledgments

The conference and its published proceedings would not have been possible without the diligent, coordinated effort of numerous people, especially the reviewers who provided detailed feedback on papers and the session chairs who made decisions and provided editorial assistance on selected topics. The editorial team is also profoundly grateful to Dr. Daniel Pradel and Dr. Navid Jafari (Conference Co-Chairs), the Technical Program Committee (listed below), Mr. Brad Keelor, Ms. Aurora Phlegar, and the ASCE publications team for their crucial roles in the production of these proceedings.

**Geo-Extreme 2025 Conference Program Committee**

Conference Co-Chairs

- Daniel Pradel, Ph.D., P.E., M.ASCE, *Ohio State University*
- Navid H. Jafari, Ph.D., M.ASCE, *Texas A&M University*

Technical Program Committee

- Timothy D. Stark, Ph.D., P.E., BC.GE, F.ASCE, *University of Illinois at Urbana-Champaign*
- James A. McKelvey, III, Ph.D., P.E., BC.GE, F.ASCE, *Earth Engineering Incorporated*
- Jeremy Varner, P.E., M.ASCE, *Federal Energy Regulatory Commission*
- Nazli Yesiler, Ph.D., A.M.ASCE, *California Polytechnic State University, San Luis Obispo*
- Ghada Ellithy, Ph.D., P.E., M.ASCE, *Embry-Riddle Aeronautical University*
- Stefan G. Flynn, P.E., M.ASCE, *US Army Corps of Engineers, Rock Island District*

Proceedings Editors

- Christopher L. Meehan, Ph.D., P.E., BC.GE, F.ASCE, *University of Delaware*
- James A. McKelvey, III, Ph.D., P.E., BC.GE, F.ASCE, *Earth Engineering Incorporated*
- Adda Athanasopoulos-Zekkos, Ph.D., M.ASCE, *University of California, Berkeley*
- Miguel A. Pando, Ph.D., P.Eng., M.ASCE, *Drexel University*
- Nina Stark, Ph.D., M.ASCE, *University of Florida*
- Ming Xiao, Ph.D., P.E., BC.GE, F.ASCE, *Pennsylvania State University*

© ASCE

# Contents

*Soil-Structure Interaction*

**Assessment and Design Considerations for Tunnel Linings in Fault Zones Subject to Rubble-Induced Loading Using 2D and 3D Numerical Modeling ..... 1**
Mohammad Moridzadeh

**Overcoming Stiff Clay Anchoring Challenges through Vibratory Installation with a Deeply Embedded Ring Anchor ..... 10**
Song Qin, Junho Lee, and Charles P. Aubeny

**Modeling Suction Bucket Foundations under Cyclic Loading through a Coupled Nonlocal Meshless Paradigm ..... 20**
Hossein Pashazad and Xiaoyu Song

**Finite Element Modeling of Soil-Foundation-Structure Interaction for Seismic Performance of Nuclear Power Plants ..... 30**
Lei Wang and Skarleth Gutierrez

**Seismic Vulnerability Assessment of RC Buildings Considering Soil-Structure Interaction Effects with Mohr-Coulomb and Hardening Soil Models ..... 38**
Pranoy Debnath, Hamzah M. B. Al-Hashemi, and Deepankar Choudhury

**Experimental Behavior of Structurally Different Pile Foundations ..... 51**
Will P. Shaffer, Rabie Farrag, Carter Cox, and Anne Lemnitzer

*Embankments, Dams, Levees, and Slopes*

**Effect of Pore Water Salinity on the Residual Strength of Bentonite ..... 61**
Mohammadreza Jebeli, Siamak Yoosefi, and Christopher L. Meehan

**Quantitative Assessment of Levee Breach Widening and Time-Rate Volume Loss Using Historical Overtopping Events ..... 70**
Stefan Flynn, April Bowman, and Farshid Vahedifard

**Large Deformation and Critical State Analysis of the Fundão Tailings Dam ..... 80**
Alomir H. Favero Neto, Gustavo R. A. Oliveira, Leandro L. Rasmussen, and Erick Rógenes

**Modeling Thermal Slope Failure through a Nonlocal THM Meshless Paradigm ..... 90**
Hossein Pashazad and Xiaoyu Song

© ASCE

**Seepage Dynamics of Geosynthetic-Reinforced Dikes under Normal and Extreme Wave Conditions in Coastal Louisiana.....100**
Abhishek K. Tiwari and Jay X. Wang

**Probabilistic Analysis of a Landslide under an Extreme Rainfall Considering Spatial Variability of Soil Strength and Hydraulic Parameters.....111**
Leila Baninajarian, Sina Javankhoshdel, and Rashid Bashir

***Geomaterials***

**Fracture Angularity Influence on Failure Behavior of Grouted Rocks for Geohazard Mitigation .....123**
Matthew O. Sonibare and Oladoyin Kolawole

**Shake Table Studies of a Geotechnical Seismic Isolation System Using Lightweight Aggregates .....130**
Farzad Naseri, Farmehr M. Dehkordi, and Fariborz M. Tehrani

**Performance Assessment and Numerical Simulation of Geo-Materials in Civil Infrastructure Subjected to Typical Loading Conditions.....139**
Sultan Almuaythir, Muhammad S. I. Zaini, and Norhaliza Wahab

**Considerations of Undrained Behavior of Compacted Clay Embankments under Extreme Wetting-Drying Cycles .....148**
Ghada Ellithy and John F. Peters

**Role of Frequency on the Cyclic Compression Response of Tire-Derived Aggregate.....155**
Mayalia E. Guntle, Axel A. Yarahuaman, and John S. McCartney

***Pipeline Behavior during Extreme Events***

**Estimation of Permanent Ground Displacement Demand on Pipelines Buried in Organic Soils .....166**
Prajakta Jadhav, Thushara Jayasinghe, and Dharma Wijewickreme

**Mechanical Performance of Rehabilitated Pipelines Using Trenchless Technologies under External Loading .....174**
Sina G. Senji, Brad P. Wham, and Shideh Dashti

**Response of Buried Pipelines Subjected to Abrupt Block Ground Movements .....184**
Auchib Reza and Ashutosh S. Dhar

© ASCE

**Analytical Method for Assessing Buried Pipeline Performance under Large Ground Movements** ..... **195**
Hailey-Rae Rose and Brad P. Wham

*Case Histories of Retaining Structures, Excavations, and Slopes*

**Landslide Identification and Proposed Remediation for Castaic Power Plant South Portal Access Road** ..... **205**
Anthony Dombrowski, Jennifer Vanegas, Liping Yan, and Cesar Larios

**Case Study on Excessive Displacements of MSE Wall and Retained Backfill due to the Cumulative Effects of Tropical Rainfall** ..... **219**
Jose Carlo Eric L. Santos and Joanne Marie P. Vizcarra

**Settlement Control of a Massive Underground Tank Resting on Uncontrolled Rock Fill: A Case Study** ..... **228**
M. E. Al-Atroush

**Case Study: Deep Interceptor Sewer Replacement in an Urban Area** ..... **246**
Issa S. Oweis and Eric Granholm

**Methodologies for Effective Slope Failure Reconnaissance** ..... **261**
Pavlo Chrysovergis, Taki Chrysovergis, and Stavros Chrysovergis

**Trump National Golf Club—25 Years after a 17 Acre Landslide Destroys the 18th Hole in Rancho Palos Verdes** ..... **270**
Richard Sack

**Stabilization of Storm-Caused Landslide with Fast Pressed-In Pipe Pile Wall Installation** ..... **281**
Takefumi Takuma and Masafumi Yamaguchi

*Case Histories Involving Extreme Loading Associated with Earthquakes*

**Validating Liquefaction Case Histories Using Earthquake Simulations: 1933 Long Beach Earthquake** ..... **290**
Sajan K C and Chukwuebuka C. Nweke

**Lessons Learned from the 2011 Tohoku Earthquake: Challenges and Innovations in Disability-Inclusive Infrastructure and Preparedness** ..... **300**
Mihoka Fukurai and Lisa Grant Ludwig

**Lessons Learned from Site Characterization Efforts during Reconnaissance: 2022 Taitung Earthquakes** ..... **314**
Rashid Shams and Chukwuebuka C. Nweke

© ASCE

**Performance of Small-Diameter Deep Foundations during the March 11, 2011, Tohoku Earthquake ..... 323**
Daniel Pradel

**Evaluating Site Response Analysis at Liquefiable Sites in the New Madrid Seismic Zone: Challenges and Lessons Learned ..... 338**
Matteo Montesi and Rachel Reardon

**Geosynthetic Solutions for Soft Soil Foundations in Seismic Regions: A Case Study of GECs below a Reservoir ..... 353**
Carlos M. Rodriguez, Vona M. Ojaruega, and Vincent Ogunro

***Soil Properties***

**Effect of Pore Fluid Salinity on Atterberg Limits of Three Types of Clay: Bentonite, Kaolinite, and a Natural Lean Clay ..... 364**
Siamak Yoosefi, Mohammadreza Jebeli, William J. Baker III, and Christopher L. Meehan

**Evaluating the Effect of Pore Fluid Salinity on the Volume Change Behavior of Bentonite Clay ..... 373**
Siamak Yoosefi, Mohammadreza Jebeli, and Christopher L. Meehan

**Mechanical and Hydraulic Characteristics of Residual Soils in the Indian Himalayas under Repeated Hydraulic Cycles ..... 383**
Eedy Sana and Ashutosh Kumar

© ASCE

# Assessment and Design Considerations for Tunnel Linings in Fault Zones Subject to Rubble-Induced Loading Using 2D and 3D Numerical Modeling

Mohammad Moridzadeh, Ph.D., P.E., M.ASCE[1]

[1]Stantec, Chicago, IL. Email: mohammad.moridzadeh@stantec.com

## ABSTRACT

This paper discusses design considerations and analyses for evaluating the behavior of tunnel linings within fault and shear zones. The materials above a tunnel passing through shear zones are prone to collapse during construction, potentially creating a cavity above the tunnel that may later be filled with rubble, increasing the load on the lining. This study examines how the rubble affects the integrity and stability of the lining, and how its impact can be assessed using two- and three-dimensional Finite Element (FE) analyses. The discussion covers deformations, forces, and bending moments in the lining, as well as the arching factor, which is calculated by comparing the results of 2D and 3D models. Recommendations for enhancing the long-term stability of the lining are also provided.

## INTRODUCTION

The construction of tunnels in shear zones presents significant challenges due to the geological complexity of these areas. The tunnels designed and constructed through a mountainous terrain require extensive excavation work through various rock formations. Tunnels can be constructed using conventional drill-and-blast techniques to overcome various geological challenges, such as rock mass deformations and instabilities. Various support structures and reinforcement techniques are employed to help the tunnel stability. However, tunnels may still experience instabilities during construction. These instabilities are often attributed to geological complexities. Given the challenges posed by the geological site conditions including significant faults, joint sets, and variable rock masses, it is critical to use advanced techniques such as numerical modeling to simulate the tunnel behavior and understand the causes of instabilities. Such methods have been previously utilized to successfully model underground structures in challenging ground conditions (Ghaboussi, et al. 1973; Bfer, 1985; Moridzadeh and Disckson, 2018; Moridzadeh and Quiroz, 2018). Interface elements were successfully used by Moridzadeh et al. (2019) to analyze large deformations occurring in the roof of caverns. Other studies have also used interface elements to analyze the stability of underground structures in a fractured rock mass (Ma et al., 2021; Moridzadeh, 2024; Xu et al., 2025).

The complex geological site conditions considered herein include joints with clay infillings and faults. The faults are perpendicular to the orientation of the tunnel axis. These faults can significantly impact the tunnel stability, leading to deformations, and a potential collapse. The varying widths of the faults can further complicate the design and construction of the tunnel.

## TUNNEL BLOCKAGE

Figure 1 shows a typical collapse that may occur during the tunnel construction along a fault zone. The material collapsing into the tunnel can form a cavity above the tunnel. In this case, the

© ASCE

collapse chimney was originally estimated to be 16.8 m above the tunnel, as shown in Figure 2. The tunnel was advanced through the collapsed material by pre-supporting the roof using micropiles and grouting forepoling. Tunnel support consisted of lattice girders and a 25 to 35-cm thick reinforced shotcrete lining. Additional analyses were deemed necessary to assess the impact of the collapsed material on the long-term stability of the tunnel lining. The analysis results and recommendations to maintain the long-term stability of the tunnel are presented herein.



**Figure 1. Material in a shear zone collapsed into a tunnel**

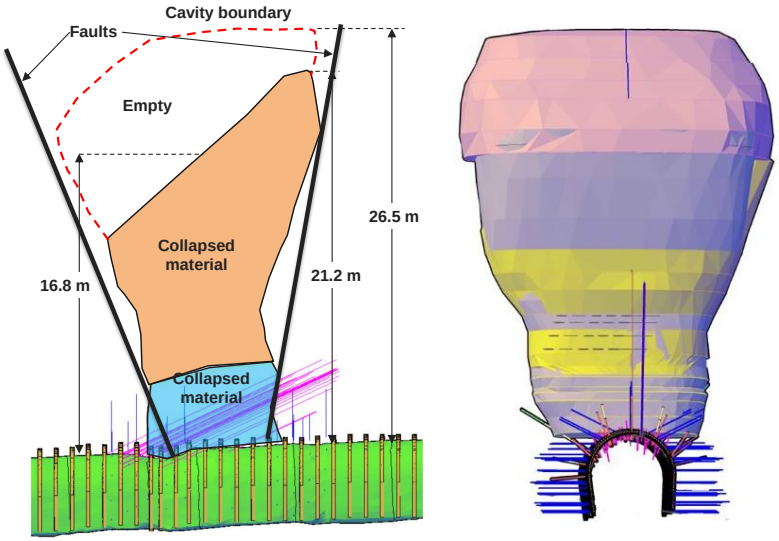



**Figure 2. Geometry of cavity along and perpendicular to tunnel**

## MATERIAL PROPERTIES

The properties of the rock, rubble, and micropile-reinforced areas utilized in the analysis are presented in Table 1. The Generalized Hoek-Brown criterion was used to model the rock in the

© ASCE

shear zone. The other materials, i.e., rubble and micropile area, were modeled using the Mohr-Coulomb criterion. An interface was defined between the rock and rubble with a frictional angle of 40 degrees and no cohesion.

**Table 1. Material properties**

| Parameter | Rock in Shear Zone | Rubble | Micropile Area – During Construction | Micropile Area – Long Term |
|---|---|---|---|---|
| Thickness Above Tunnel | - | - | 2.25 m | 2.25 m |
| Unit Weight (kN/m$^3$ | 27 | 22 | 22 | 22 |
| Young's Modulus (MPa) | 913.4 | 30 | 930 | 200 |
| Poisson's Ratio | 0.2 | 0.2 | 0.2 | 0.2 |
| Compressive Strength (MPa) | 20 | - | - | - |
| mb Parameter | 0.402 | - | - | - |
| s Parameter | 0.000138 | - | - | - |
| a Parameter | 0.544 | - | - | - |
| Friction Angle (deg.) | - | 40 | 40 | 40 |
| Cohesion (MPa) | - | 0 | 0 | 0 |

The thickness of the lining varies around the tunnel, as shown in Figure 3. The thickness was estimated to be 65 cm for below the springline (TR1 to TR3) and 35 cm above the springline (TR4 and TR5).

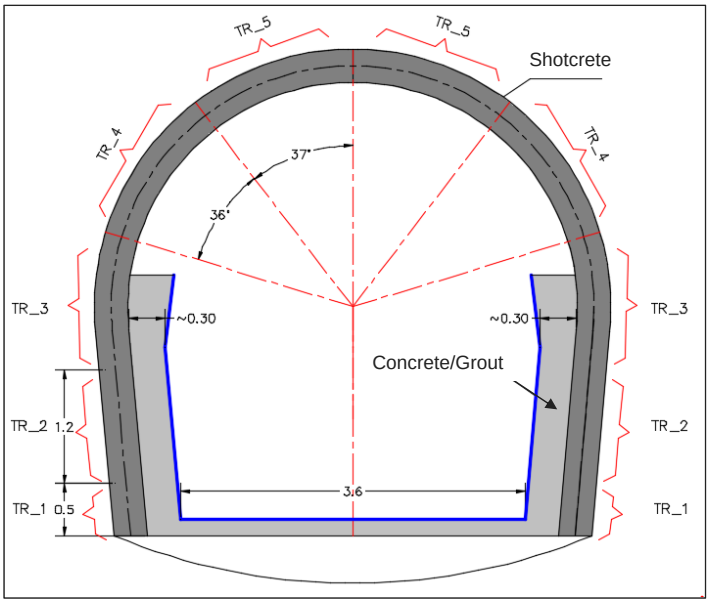



**Figure 3. Tunnel lining thickness**

## METHODOLOGY

A series of analyses were conducted using the RS2 software (RocScience, 2019) to determine the deformations, axial load, shear load, and bending moments in the tunnel lining. The details of

© ASCE

the RS2 model are shown in Figure 4. Based on the modeling results, a structural assessment was carried out to determine the adequacy of the tunnel lining. Four loading cases were assessed to understand the impact of arching effects in the rubble (collapsed) material above the tunnel as follows:

- Case 1: Rubble up to 16.8m above the tunnel
- Case 2: Rubble up to 21.2m above the tunnel
- Case 3: Rubble up to 28.3m above the tunnel
- Case 4: Rubble up to 35m above the tunnel

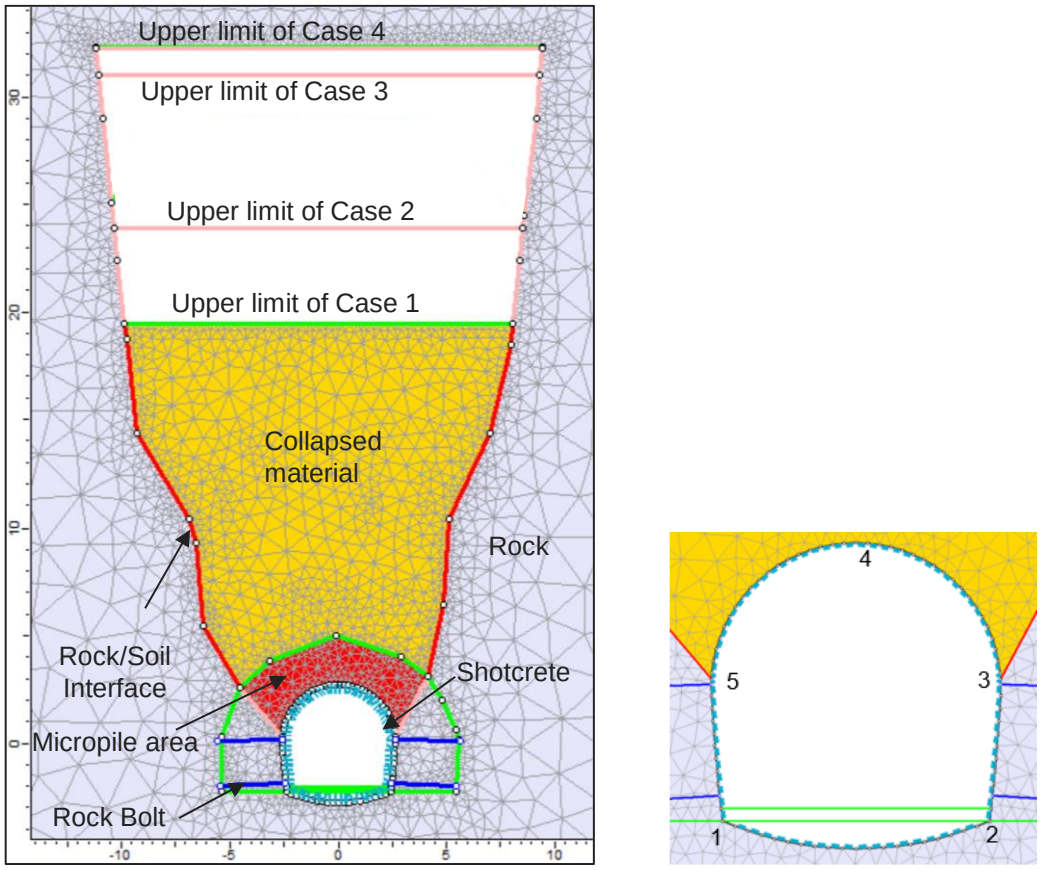



**Figure 4. Characteristics of RS2 model (2D)**

Drained conditions were utilized to assess the long-term stability of the lining. The horizontal stress ratio ($k_0$) was iteratively determined as 0.15 by matching the modeled and actual tunnel displacements at the end of construction. To realistically account for the construction sequence and the distribution of stresses around the tunnel, the model was set up using the following stages:

- Stage 1: In-situ conditions (pre-excavation)
- Stage 2: Installation of micropiles above the tunnel crown
- Stage 3: Excavation of the tunnel and changing the rock inside the cavity to rubble up to a height of 16.8m above the tunnel (Case 1 geometry)
- Stage 4: Installation of tunnel support elements (shotcrete and rock anchors)

© ASCE

- Stage 5: Change the short-term material properties to those for the long-term condition of the micropile zone above the tunnel
- Stage 6: Remove the micropile zone (change to rubble) for Case 1 geometry
- Stage 7: Increase the height of rubble above the tunnel corresponding to the Case 2 geometry
- Stage 8: Increase the height of rubble above the tunnel corresponding to the Case 3 geometry
- Stage 9: Increase the height of rubble above the tunnel corresponding to the Case 4 geometry

Subsequently, the tunnel was modeled in three dimensions using the Ansys software (Ansys, 2019) to examine 3D effects, as shown in Figure 5. The rock was modeled as a weightless material to remove the in-situ stresses on the lining. The materials were considered to remain in the elastic range and a friction angle of 40 degrees (no cohesion and tensile strength) was used for the interface between the rubble and rock.

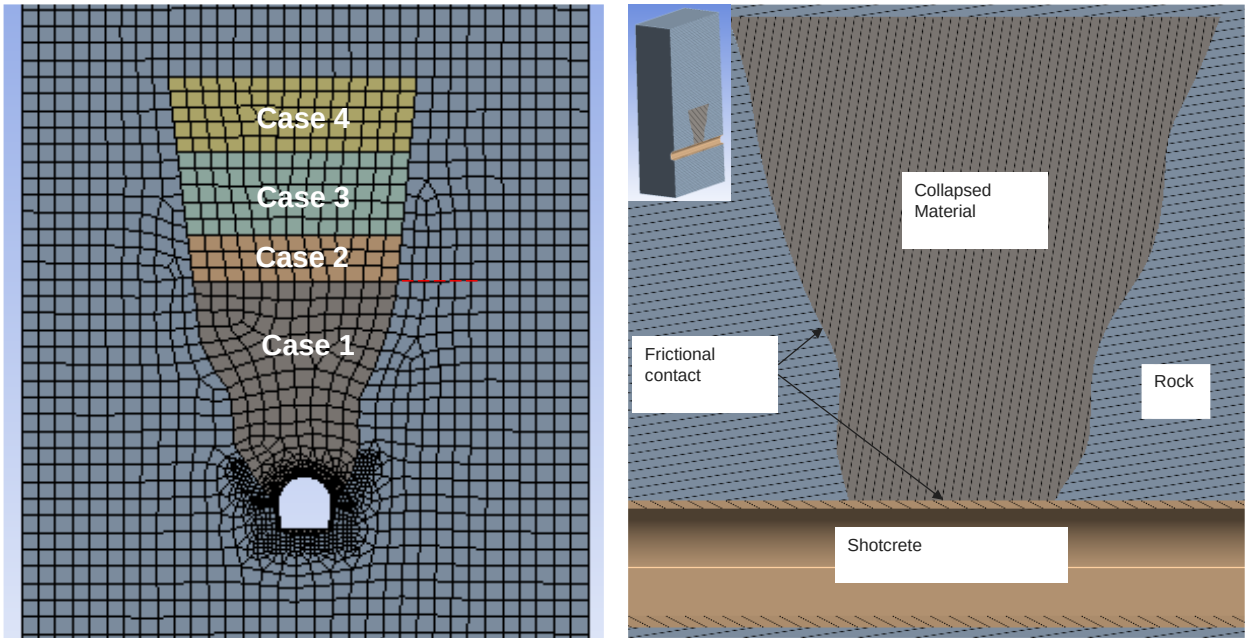



**Figure 5. 2D and 3D Ansys Models**

## RESULTS

The horizontal and vertical displacements of the lining around the tunnel are shown in Figure 6. The lining axial force, shear, and bending moment are shown in Figure 7 and the change in the lining forces and moments with the rubble height is shown in Figure 8.

## ARCHING EFEECT IN LONGITUDINAL DIRECTION

The arching effect was evaluated by comparing the results of the 2D and 3D Ansys models, as shown in Figure 9. The arching factor was calculated as the ratio of the reaction force on the

© ASCE

lining calculated from the 3D model (0.95 MN/m) to that from the 2D model (1.47 MN/m). The calculated ratio of 0.65 indicated that 35% of the load is distributed in the longitudinal direction. This assumes that the load is uniform along the tunnel. However, the load is distributed in both transversal and longitudinal directions. The axial force at the connection of the arch to the walls was calculated to determine the proportion of the load distributed in both directions. The maximum axial force is 0.44 MN/m at each side. The total lining load is calculated to be 0.88 MN/m, hence a second reduction factor of 0.88 MN/m / 0.95 MN/m = 0.93 is calculated. This factor indicates that the axial force from the 3D analysis is 93% of the load on the lining. The remaining 7% is transferred through shear in the longitudinal direction. Combining the two effects, a ratio of 0.65 x 0.93 = 0.6 is calculated. By applying this ratio to the results of the 2D model, those of the 3D model accounting for the arching effect in the longitudinal direction can be obtained.

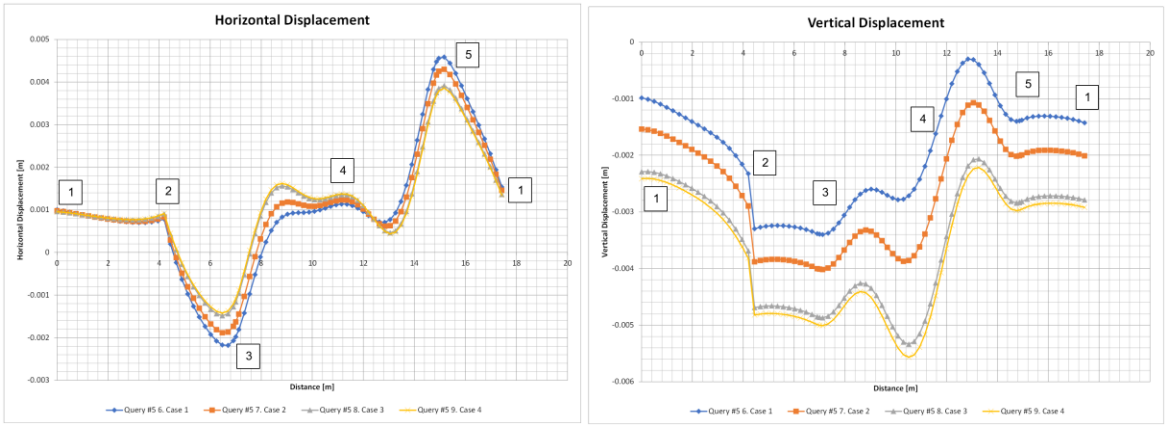



**Figure 6. Horizontal and vertical displacements of lining without micropiles**

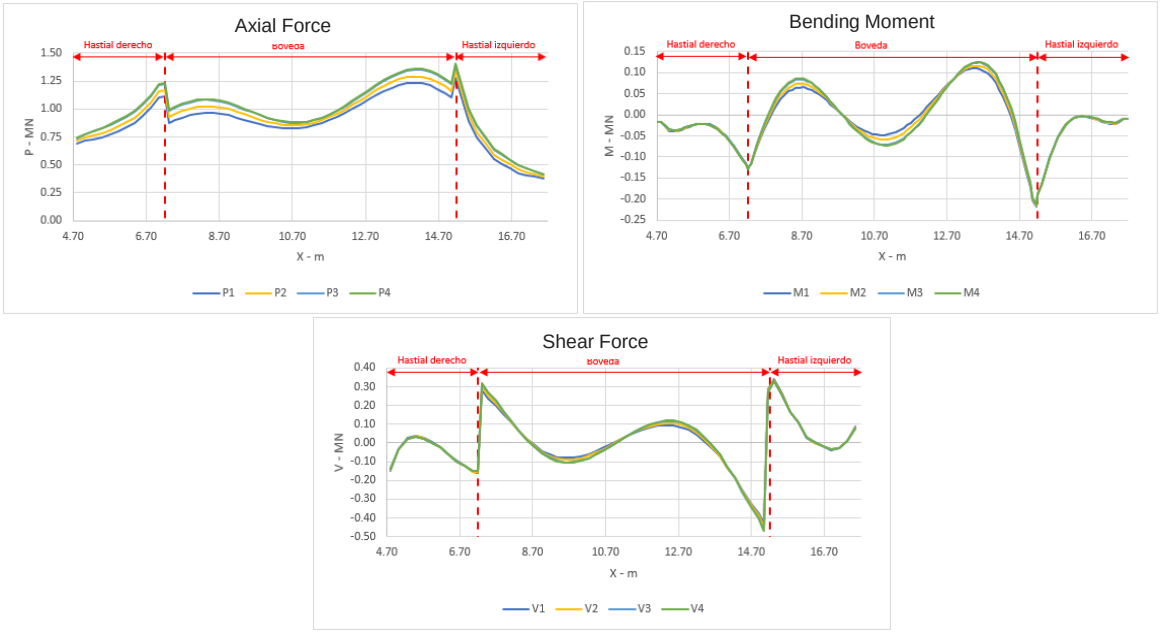



**Figure 7. Lining forces and moments for permanent condition without micropiles**

© ASCE

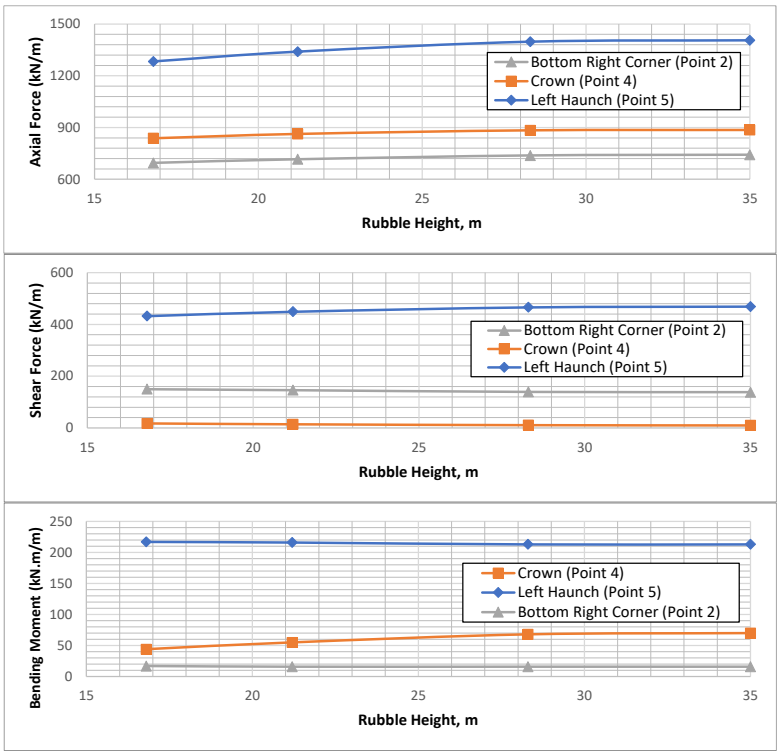
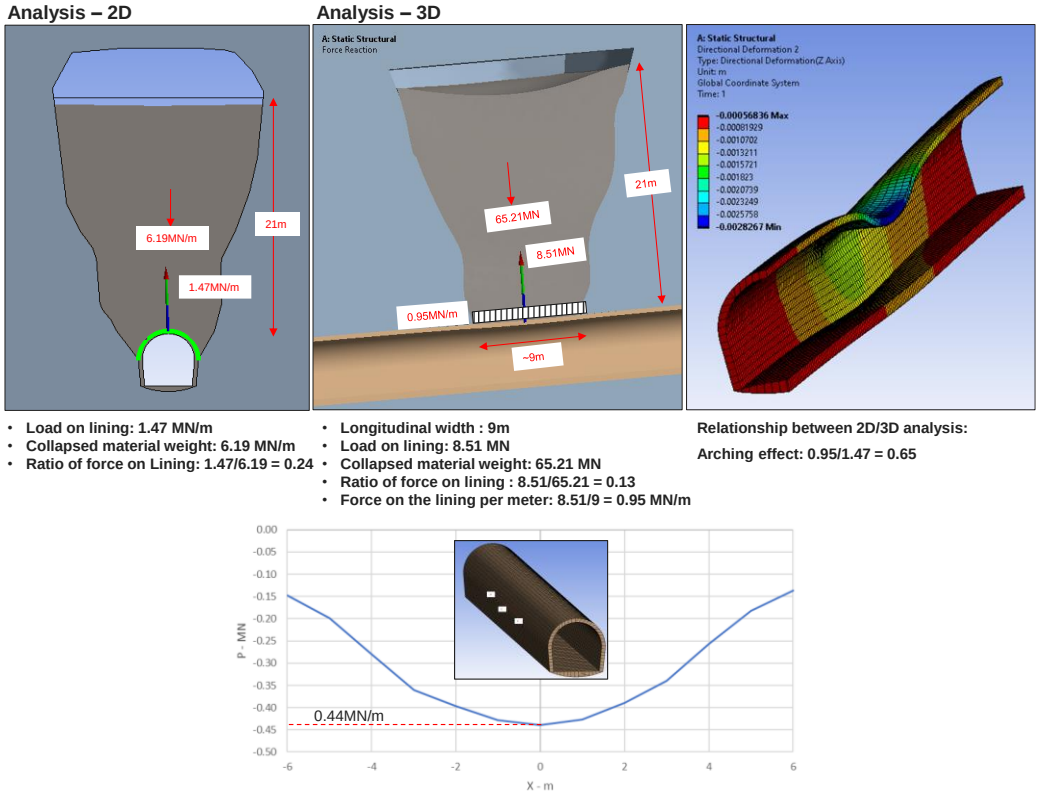



**Figure 8. Change in Lining forces and moments with rubble height**




- Load on lining: 1.47 MN/m
- Collapsed material weight: 6.19 MN/m
- Ratio of force on Lining: 1.47/6.19 = 0.24

- Longitudinal width : 9m
- Load on lining: 8.51 MN
- Collapsed material weight: 65.21 MN
- Ratio of force on lining : 8.51/65.21 = 0.13
- Force on the lining per meter: 8.51/9 = 0.95 MN/m

Relationship between 2D/3D analysis:

Arching effect: 0.95/1.47 = 0.65

**Figure 9. Arching effect from Ansys models**

© ASCE

## CONCLUSION AND RECOMMENDATIONS

A series of numerical analyses were performed to evaluate the performance of a tunnel lining due to a collapse that formed a cavity above it. Based on the analyses, the following conclusions are drawn:

- As the height of the rubble in the cavity increased, the impact on the lining forces and bending moment was minimal due to the arching effect.
- The maximum values occurred at Point 5 (right haunch) for cases without micropiles.
- To take into consideration the effect of longitudinal load transfer in 3D on the results of the 2D models, a reduction factor of 0.6 was applied to the 2D analysis results.
- The 3D case is deemed to be more realistic and representative of the site condition.
- Routine inspection and monitoring of the tunnel is necessary. It is recommended that the tunnel lining be inspected, and the thickness and strength of the shotcrete be verified in the field. The following steps are taken to determine the required lining modifications:
    1. Perform tunnel inspection
    2. Verify shotcrete properties including thickness, strength, and density
    3. Monitor the tunnel convergence
    4. If shotcrete properties required for the lining stability are verified and convergence is minimal, no modifications are needed. Otherwise, the lining needs to be reinforced. The minimum required lining properties are as follows:
        a. Thickness of 35 cm
        b. Strength of 25 MPa
        c. Density of 2300 kg/cm3
- If a minimum thickness of 35 cm with the above properties is confirmed, the structural minimum factor of safety will be met. Otherwise, at least 15 cm of additional shotcrete is required at the crown and haunches.

## REFERENCES

Ansys. (2019). *Finite element software, Ansys, Inc, version 19.5*.

Bfer, G. (1985). "An isoparametric joint/interface element for finite element analysis." *International Journal for Numerical Methods in Engineering*, 21(4): 585-600.

Ghaboussi, J., Wilson, E. L., and Isenberg, J. (1973). "Finite element for rock joints and interfaces." *Journal of the Soil Mechanics and Foundations Division*, ASCE, 99(10): 849-862.

Ma, S., Zhang, L., Wang, D., Tan, X. R., Li, S., and Liu, Y. (2021). "Analysis of tunnel lining failure mechanism under the action of active fault." *Shock and Vibration* 2021, no. 1: 9918021.

Moridzadeh, M., and Dickson, P. (2018). "Design methodology to evaluate hydraulic jacking in pressure tunnels." *Proceedings of International Foundation Congress and Equipment Expo (IFCEE)*, Orlando, March 5-10, 2018.

Moridzadeh, M., and Quiroz, J. (2018). "Hydraulic jacking analysis of pressure tunnels using coupled hydromechanical finite element and discrete element approaches." *Proceedings of ITA World Tunnel Congress (WTC)*, Dubai, April 21-26, 2018.

Moridzadeh, M., Djavid, M., and Doyle, B. (2019). "Stability assessment of large caverns in horizontally bedded strata considering time-dependent response." *Proceedings of Geo-Congress: Eighth International Conference on Case Histories in Geotechnical Engineering*, Philadelphia, March 24-27, 2019.

© ASCE

Moridzadeh, M. (2024). “Three-dimensional coupled stress and fluid flow analysis and design provisions for Lake Mead Intake No.3 Low Level Pumping Station in fractured rock mass.” *Proceedings of Geo-Congress*, Vancouver, February 25-28, 2024.

Rocscience. (2019). *2D Finite element analysis software RS2*, *version 9.0*.

Xu, L., Du, X., Huang, J., Zhao, M., El Naggar, M. H., and Zhao, X. (2025). “Generalized solution for tunnel longitudinal response to fault movement.” *Soil Dynamics and Earthquake Engineering* 190: 109230.

**© ASCE**

# Overcoming Stiff Clay Anchoring Challenges through Vibratory Installation with a Deeply Embedded Ring Anchor

Song Qin[1]; Junho Lee, Ph.D.[2]; and Charles P. Aubeny, Ph.D., P.E., F.ASCE[3]

[1]Zachry Dept. of Multidisciplinary Engineering, Texas A&M Univ., College Station, TX. Email: qinsong@tamu.edu
[2]Deep Anchor Solutions Inc., Houston, TX. Email: geojunho@gmail.com
[3]Zachry Dept. of Civil and Environmental Engineering, Texas A&M Univ., College Station, TX. Email: caubeny@civil.tamu.edu

## ABSTRACT

Floating solar plants offer a renewable energy solution in areas with limited land space, but they face challenges such as strong winds and wave forces. Reliable anchoring is crucial for stability, but traditional methods like ground anchoring are limited in stiff clay soil due to low drainage and high cohesion. The Deeply Embedded Ring Anchor (DERA), designed for deep-water use, offers enhanced holding capacity, a compact design, and resilience against extreme conditions, making it suitable for floating solar installations in clayey soils. However, conventional suction installation faces limitations in shallow waters due to insufficient hydrostatic pressure and cavitation risks. Vibratory installation is proposed as an alternative, enabling effective anchor embedment in shallow waters. Challenges include clay's high cohesion and stiffness, requiring careful optimization of vibratory force and equipment. A study developed a vibratory installation model for clay soil, validating it with real-world data and conducting parametric studies to assess performance across various anchor sizes and soil profiles.

## INTRODUCTION

Floating solar plants offer an effective renewable energy solution in areas with limited land availability. However, their deployment presents significant engineering challenges, especially in anchoring systems that must withstand extreme environmental forces like wind and hydrodynamic loads. A reliable anchoring solution is essential for ensuring stability and long-term performance (Lee et al. 2021, 2025). A key challenge in anchoring floating solar plants is the soil condition at deployment sites. Many systems are installed in shallow waters, where soft clay dominates due to recent sedimentation and low consolidation (Mesri and Olson 1971, Santamarina et al. 2001). However, stiff clay deposits can also be encountered, particularly in areas with over-consolidated marine clay or long-term deltaic sediment compression (Locat and Demers 1988, Bjerrum 1973). These soil conditions create challenges for traditional anchoring methods, requiring alternative installation techniques optimized for stiff clay in shallow waters.

Traditional anchoring methods, such as driven piles and screw anchors, can face increased resistance and penetration difficulties in stiff clay due to its high cohesion and low permeability (Lutenegger 2011, Randolph and Gourvenec 2011). Driven piles may require high-energy impact hammers or predrilling to reach the necessary depth, which can generate significant noise, potentially disturbing marine mammals (Qin et al. 2025), while screw anchors often encounter torque limitations, sometimes requiring additional aids like water jetting or predrilling (Clukey et al. 2017, Perko 2009, Aubeny et al. 2005). These challenges highlight the need for innovative anchoring solutions tailored to stiff clay in shallow waters.

© ASCE

The Deeply Embedded Ring Anchor (DERA) is a high-capacity anchoring solution suitable for various soil conditions. In clay-rich seabeds, DERA is effectively installed using suction, utilizing hydrostatic pressure for deep embedment (Lee and Aubeny 2020). Suction installation is favored for its low acoustic impact, high efficiency, and strong geotechnical performance. However, in shallow waters (typically less than 20–30 meters), suction installation faces challenges due to insufficient hydrostatic pressure, which can lead to cavity formation and limit penetration depth (Clukey et al. 2017). Since floating solar plants are often deployed in such environments, alternative installation techniques are needed to achieve deep embedment without the limitations of hydrostatic pressure. Vibratory installation has been identified as a potential solution to overcome these constraints. This method applies cyclic vertical or rotational forces to mobilize the surrounding soil, reducing penetration resistance and enhancing embedment depth (Ehlers et al. 2019). While vibratory techniques are widely used in sands and soft clays, their effectiveness in stiff clay has been less explored due to concerns about high cohesion, limited drainage, and inadequate cyclic softening (White et al. 2002). However, recent studies indicate that vibratory installation can be effective in clay soils if vibratory parameters are optimized (Aubeny 2023). A newly proposed theoretical model for vibratory installation in clay shows that controlled cyclic shearing can reduce soil resistance and enable deeper penetration, even in high-cohesion materials. These findings support the feasibility of vibratory installation as a viable alternative for DERA deployment in stiff clay environments.

This study evaluates the feasibility of vibratory installation for DERA in stiff clay. A vibratory installation model is developed to estimate key parameters, such as hammer size and operating frequency. The model is validated using existing installation data, and parametric studies assess the impact of anchor size and soil properties on vibratory installation performance. The findings contribute to advancing efficient anchoring solutions for floating solar applications, addressing the challenges of shallow water deployments in stiff clay environments.

## KEY ISSUES OF VIBRATORY INSTALLATION OF DERA IN CLAY

### Key Vibratory Parameters for DERA Installation in Clay

The vibratory installation of the DERA in stiff clay depends on key parameters such as vibration frequency, amplitude, acceleration, and loading direction. However, DERA's unique ring geometry and its reliance on a follower system require a distinct approach compared to conventional piles or helical anchors.

The DERA system consists of a ring anchor (short tube) and a follower (long tube) that facilitates deep embedment (Lee et al. 2020, Lee and Aubeny 2020). During installation, the DERA is attached beneath the follower, and both advance incrementally into the seabed under vibratory loading. Once the target penetration depth is reached, the follower is detached and extracted, leaving the DERA embedded in deep soil (Figure 1).

For simplicity in analysis, the DERA-follower system is modeled as a regular steel pile with the same diameter and wall thickness. This assumption allows for a straightforward interpretation of vibratory installation behavior without the added complexity of ring-soil interaction effects. Key vibratory parameters for DERA-follower installation are as follows:

- Vibration Frequency: Unlike traditional piles, DERA experiences resistance at both the ring-soil interface and the follower-anchor connection, requiring frequency tuning for uniform penetration (White et al. 2002, Aubeny 2023).

© ASCE

- Amplitude & Acceleration: While high amplitudes enhance penetration, DERA's assumed pile-like behavior necessitates controlled amplitude settings to prevent excessive stress on the system (Ehlers et al. 2019).
- Loading Direction: While vertical vibrations are common for cylindrical piles, torsional or combined vertical-torsional vibrations may improve penetration efficiency for DERA-like structures (Ehlers et al. 2019).

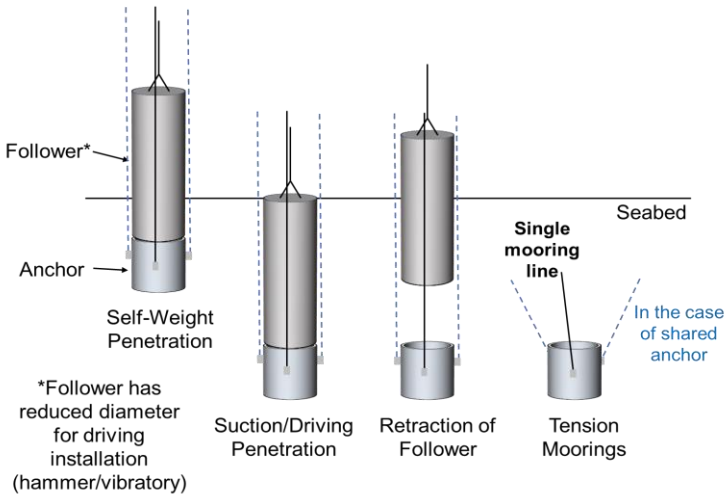



**Figure 1. DERA installation procedures (Source: Lee and Aubeny 2020).**

## Challenges and Solutions for Vibratory Installation

Vibratory installation in stiff clay presents unique challenges for the DERA-follower system, particularly given its assumption as a steel pile for analysis purposes. Unlike conventional piles, which experience penetration resistance along a linear shaft, DERA must overcome resistance at both the ring edges and the central installation follower (White et al. 2002; Aubeny 2023).

Challenges of Vibratory Installation with a Follower System are as follows:

- Energy Transfer Efficiency: Since DERA is modeled as a regular pile, vibratory energy transfer is assumed to be uniform, but losses at the follower-derivation interface may impact penetration performance (Randolph & Gourvenec 2011).
- Non-Uniform Stress Distribution: The ring-anchor structure interacts with the surrounding soil differently from a conventional pile, requiring assumptions about stress distribution to simplify analysis (Ehlers et al., 2019).
- Limited Cyclic Softening in Stiff Clay: Unlike sands, stiff clay does not undergo significant pore pressure buildup, making it necessary to consider load cycling approaches for vibratory optimization (Aubeny, 2023).

To address these challenges, this study examines vibratory installation strategies under the assumption that DERA behaves as a conventional pile. Potential strategies include:

- Adaptive frequency tuning to optimize penetration efficiency.
- Load cycling techniques to compensate for the limited cyclic softening effect in stiff clay.
- Energy transfer optimization at the follower-anchor interface to mitigate potential inefficiencies.

© ASCE

## VIBRATORY INSTALLATION MODEL

The vibratory installation model consists of three key steps. First, soil resistance is estimated at each penetration depth. Second, the hammer size and operating frequency are assumed to calculate the vibratory force. Finally, a Newmark analysis is applied to assess the penetration rate and determine drivability.

### Soil Resistance

The installation mechanism in clay soils relies on the vibratory force and system weight overcoming soil resistance. Therefore, accurately predicting soil resistance is essential. Soil resistance can be estimated using the following equation:

$$Q_{tot} = Q_{tip} + Q_{side} = N_c s_{utip} A_{tip} + \alpha s_{uavg} A_s \quad (1)$$

where $Q_{tot}$ = total resisting force; $Q_{tip}$ = tip resistance; $Q_{side}$ = side resistance; $N_c$ = end bearing factor; $A_{tip}$ = annular area of bucket tip; $s_{utip}$ = undrained shear strength at the anchor tip; $\alpha$ = adhesion factor; $s_{uavg}$ = average undrained shear strength along the current depth of the anchor and follower; $A_s$ = inner and outer surface of the embedded portion of the anchor and follower.

### Vibratory Force

During the driving process, the vibratory hammers utilize rotating mass $m_e$ with an eccentricity $e$ about the axis of rotation at a controlled frequency to generate the downward force, as presented in following equation (Jonker 1987):

$$F_d = m_e e \Omega^2 \sin \Omega t \quad (2)$$

where $F_d$ = the inertial dynamic force from vibro-driver; $m_e e$ = eccentric moment of rotating masses; Ω= angular frequency of rotating masses.

### Newmark Analysis

The effect of soil weakening caused by excess porewater pressure is negligible during vibratory installation in cohesive soils. Thus, pile penetration in clay occurs when the sum of the driving forces momentarily exceeds the soil resistance. The equilibrium can be expressed as:

$$F_d - Q_{net} = M\ddot{h} \quad (3)$$

where $Q_{net}$ = net soil resistance force = $Q_{tot}$ - $W'$ + $T$; $W'$ = system buoyant weight; $T$ = hook line tension; $M$ = system mass; $\ddot{h}$ = relative acceleration between pile and soil.

When the sum of static and dynamic driving forces exceeds soil resistance, the pile accelerates downward into the soil. Double integration of the acceleration estimates the downward displacement during a single vibration cycle. As shown in Figure 2, the net resistance is the total soil resistance minus all driving stresses, including the weight of the pile, hammer, and any attachments during penetration. This method closely follows Newmark's (1965)

© ASCE

approach for estimating permanent deformation in earth masses during seismic shaking. The time $t_1$ at which slip initiates can be calculated as follows:

$$t_1 = \frac{1}{\Omega}\sin^{-1}\left(\frac{Q_{net}}{m_e e \Omega^2}\right) \tag{4}$$

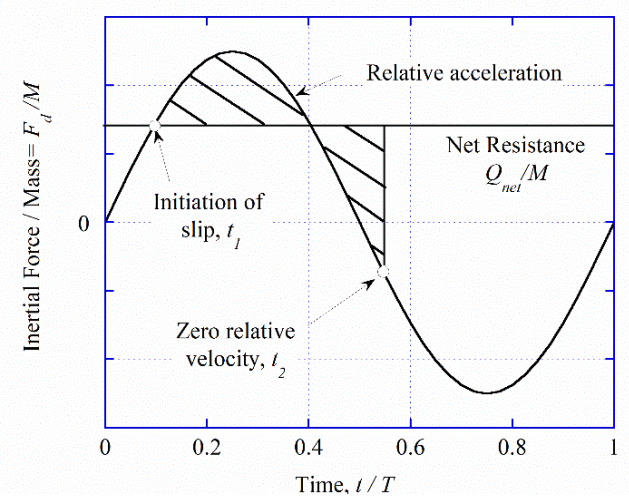



**Figure 2. Newmark analysis (Source: Aubeny 2023).**

Integrating the acceleration yields the following expression for velocity:

$$\dot{h} = \int_{t_1}^{t}\left(\frac{F_d - Q_{net}}{M}\right)dt = \frac{m_e e \Omega^2}{\Omega M}(\cos\Omega t_1 - \cos\Omega t) - \frac{Q_{net}}{M}(t - t_1) \tag{5}$$

$t_2$ is the time when slippage ceases (velocity equals zero) and can be calculated by Eq. 5. Integrating the equation of velocity produces the following equation of permanent pile penetration per load cycle:

$$\Delta h_{1cyc} = C_1(t_2 - t_1) - \frac{m_e e}{M}(\sin\Omega t_2 - \sin\Omega t_1) - \frac{Q_{net}}{2M}({t_2}^2 - {t_1}^2) \tag{6}$$

$$C_1 = \frac{m_e e \Omega}{M}\cos\Omega t_1 + \frac{Q_{net}}{M}t_1 \tag{7}$$

The average rate of pile penetration $v$ is then simply computed by multiplying the penetration distance per load cycle by frequency $f$:

$$v = \Delta h_{1cyc} f = \left(\frac{dh}{dN}\right) f \tag{8}$$

where $h$ is the penetration and $N$ is the total cycles. Pile penetration will occur so long as the dynamic force $F_d$ exceeds the net soil resistance $Q_{net}$. However, if $F_d$ - $Q_{net}$ is not sufficiently large, the penetration velocity will be unacceptably low. The recommended hammer size for pile penetration in clays is calculated using the following equation (Aubeny 2023):

© ASCE

$$(m_e e)_{min} = \frac{4Q_{net}}{\Omega^2} = \frac{4Q_{net}}{(2\pi f)^2} \quad (9)$$

## Model Validation

The Riffgat Wind Farm project in the North Sea included monopile foundations for 30 wind turbines (de Neef et al. 2013). The hammer used in the Riffgat Wind Farm project has an eccentric moment of 0.92 tonne-m (combined from 4 hammers). The installation times for all piles were under 15 minutes, indicating an average penetration rate of 22-33 mm/sec. A Newmark analysis was conducted on these pile installations, assuming an operating frequency of 23 Hz, which is likely realistic for the later stages, though a lower frequency was probably used initially. The soil type is described as stiff clay, with undrained shear strength typically between 50-75 kPa. For model validation, a uniform strength profile of 67.5 kPa was used.

Table 1 summarizes model analysis results for embedment depths of 5 to 30 meters. At 5 meters, piles can penetrate under self-weight due to low soil resistance. Predicted penetration rates are highest at shallow depths but decrease with increasing depth, reaching refusal (i.e., zero penetration rate) at full embedment. Model predictions for mid-range depths (10-20 meters) are consistent with reported average rates, ranging from 23 to 33 mm/sec. As noted in the report, impact hammers were used for the last 10 meters of installation to avoid compromising the pile's axial load capacity. Table 1 provides minimum recommended hammer sizes, which are conservative compared to the actual eccentric moment of 0.92 tonne-m. It is important to note that cyclic stress may pose a risk of fatigue failure (Qin et al. 2024). These recommendations aim to ensure acceptable penetration rates while minimizing fatigue damage by avoiding excessive load cycles.

**Table 1. Model estimates for Riffgat installation.**

| Embedment Depth (m) | Total Soil Resistance (kN) | Net Soil Resistance (kN) | Penetration Rate (mm/sec) | Req. Eccentric Moment (Tonne-m) |
|---|---|---|---|---|
| 5 | 5088 | -75 | Self-weight penetration | |
| 10 | 9172 | 4009 | 103 | 0.76 |
| 15 | 13255 | 8092 | 51 | 1.55 |
| 20 | 17339 | 12176 | 19 | 2.33 |
| 25 | 21423 | 16259 | 3 | 3.11 |
| 30 | 25506 | 20343 | Refusal | |

## APPLICATION OF THE MODEL TO DERA

This study applies the vibratory model presented above to the DERA anchors dimensioned to resist the anticipated load demand from large (15 to 20-MW) Floating Offshore Wind Turbines (FOWTs). The evaluations aim to verify that DERA installation in clays is feasible using available vibratory hammers.

© ASCE

## Study Description

Evaluating the feasibility of installing the DERA using vibratory installation requires estimates of anchor dimensions and embedment depth that are sufficiently large to provide load capacities for meeting the load demand imposed by large (15-MW or greater) floating wind turbines. As shown in Table 2, three cases of DERA installation are evaluated. The DERAs have diameters in the 2.5 to 2.9 m range. Based on previous studies, the DERA will get sufficient capacity if the penetration depth reaches 15 times the anchor diameter *D*. Accordingly, the total length of the DERA-follower system equals 15*D*. The study estimates the penetration rates at varied penetration depths of the DERAs installed by three combined APE 600 vibratory hammers (total eccentric moment equals 0.59 tonne-m) with 23 Hz operating frequency. The anchor diameter *D* to wall thickness *t* ratio is 120. The soil type is assumed to be uniform stiff clay with undrained shear strength varying from 50 to 75 kPa. The bearing factor for tip resistance $N_c$ and adhesion factor for side resistance $\alpha$ is set as 9 and 0.3. The adhesion factor is typically taken as the inverse of the sensitivity factor *St*, which commonly ranges from 2 to 5. Therefore, a value of 0.3 is used as a representative average for the adhesion factor.

**Table 2. Inputs of vibratory installation model**

| | | |
|---|---|---|
| **Case 1** | Anchor Diameter | 2.5 m |
| | Total Length | 37.5 m |
| **Case 2** | Anchor Diameter | 2.7 m |
| | Total Length | 40.5 m |
| **Case 3** | Anchor Diameter | 2.9 m |
| | Total Length | 43.5 m |
| **Soil** | Description | Uniform clay |
| | Undrained Shear Strength | 50, 60, 67.5, 75 kPa |
| **Hammer** | Model | APE 600 |
| | Eccentric Moment | 0.59 tonne-m (combined from 3 hammers) |
| | Operating Frequency | 23 Hz |

## Results

Table 3 presents the results from the vibratory installation analysis. As expected, the estimated penetration rates decrease with increasing depth. The estimates indicate that all three DERA anchors can achieve the target embedment depth using three combined APE 600 hammers, maintaining an acceptable penetration rate. The relatively high penetration rates for Cases 1 and 2 suggest that the estimated hammer size (0.59 tonne-m) is conservative. The estimated penetration rates are based on the maximum hammer operating frequency, though a lower frequency could be used for shallow depths.

Figure 3 illustrates the effect of DERA size and soil strength on the penetration rate during the final stage of vibratory installation. The data shows a significant reduction in penetration rate as anchor diameter increases. For example, the penetration rate for a DERA with a 2.9-meter diameter can drop to as low as 5 mm/sec (Figure 3a), mainly due to higher soil resistance from

© ASCE

the larger anchor size and deeper penetration. Therefore, selecting the appropriate vibratory hammer size and frequency is crucial for installing larger DERAs. Additionally, Figure 3b demonstrates that the penetration rate significantly decreases as soil strength increases. The results indicate that a large anchor size coupled with strong soil can cause installation refusal and instability, necessitating a larger vibratory hammer or higher operational frequency. This underscores the importance of vibratory installation analysis in stiff clay.

**Table 3. Vibratory model predictions.**

| | Embedment Depth (m) | Total Soil Resistance (kN) | Net Soil Resistance (kN) | Penetration Rate (mm/sec) | Req. Eccentric Moment (Tonne-m) |
|---|---|---|---|---|---|
| Case 1 | 10 | 3254 | 2841 | 923 | 0.54 |
| | 20 | 6163 | 5751 | 410 | 1.10 |
| | 30 | 7753 | 7341 | 227 | 1.40 |
| | 37.5 | 8946 | 8534 | 128 | 1.63 |
| Case 2 | 10 | 3523 | 3003 | 704 | 0.58 |
| | 20 | 6914 | 6394 | 261 | 1.22 |
| | 30 | 8631 | 8112 | 127 | 1.55 |
| | 40.5 | 10435 | 9915 | 40 | 1.90 |
| Case 3 | 10 | 3793 | 3149 | 548 | 0.60 |
| | 20 | 7452 | 6808 | 180 | 1.30 |
| | 30 | 9547 | 8904 | 66 | 1.71 |
| | 43.5 | 12038 | 11394 | 5 | 2.18 |

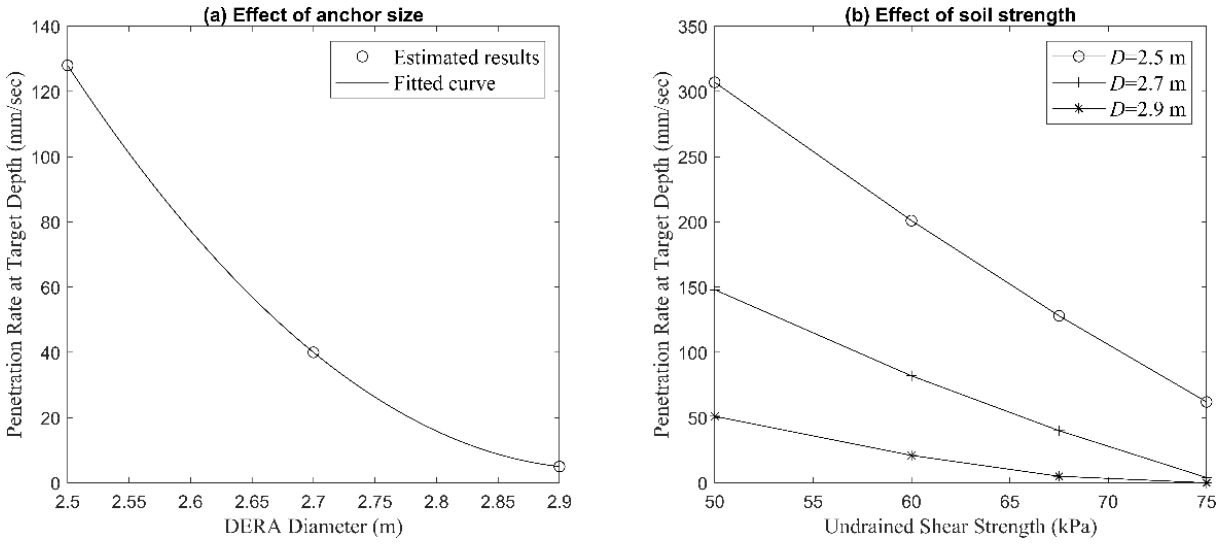



**Figure 3. Effect of DERA size and soil strength on the installation performance.**

© ASCE

## CONCLUSION

This study evaluated the feasibility of DERA-follower installation in clays using vibratory hammers. A reliable model was applied to assess the drivability with estimated hammer size and operation frequency. Significant conclusions from this study include the following:

- The vibratory installation model, with its ability to predict the penetration rate at varied installation stages, has practical implications. The results of this study have confirmed that the DERA can be advanced to the target depth in stiff clay using currently available vibratory hammer types.
- The recommended hammer size by the model appears conservative. However, it is based on avoiding possible fatigue damage due to the large number of load cycles.
- The size of the DERA and the strength of the soil can greatly influence vibratory installation performance. Larger anchors and stiff clay can impede installation, requiring careful optimization of the vibratory installation process.

## ACKNOWLEDGMENT

The authors would also like to acknowledge the support from the National Science Foundation, award numbers CMMI-1936901 and TI-2214009, and the Department of Energy, award number DE-SC0040602 and DE-EE0011636.

## REFERENCES

Aubeny, C. “Vibratory installation of bucket foundations.” *Ocean Engineering* 273 (2023): 113895.

Aubeny, C. P., H. Shi, and J. D. Murff. “Collapse loads for a cylinder embedded in trench in cohesive soil.” *International Journal of Geomechanics* 5, no. 4 (2005): 320-325.

Bjerrum, L. (1973). “Problems of soil mechanics and construction on soft clays.” *Proceedings of the 8th International Conference on Soil Mechanics and Foundation Engineering*, Moscow, 3, 111-159.

Clukey, E. C., H. Dendani, and R. Phillips. (2017). “Suction Pile Performance in Deepwater and Shallow Water Applications.” *Offshore Technology Conference*.

De Neef, L., P. Middendorp, and J. Bakker. “Installation of monopiles by vibrohammers for the Riffgat Project.” *Pfahlsymposium Proceedings of the Institute for Soil Mechanics and Foundation Engineering*, Technische Universität Braunschweig, Germany (2013).

Ehlers, S., K. I. Skau, and G. Ottesen. (2019). “Installation of Anchors in Clay Using Vibratory Driving Methods.” *Geotechnical Engineering Journal*, 45(2), 123-135.

Jonker, G. “Vibratory pile driving hammers for pile installations and soil improvement projects.” In *Offshore Technology Conference*, pp. OTC-5422. OTC, 1987.

Lee, J., and C. P. Aubeny. “Multiline Ring Anchor system for floating offshore wind turbines.” In *Journal of Physics: Conference Series*, vol. 1452, no. 1, p. 012036. IOP Publishing, 2020.

Lee, J., K. Balakrishnan, C. P. Aubeny, S. Arwade, D. DeGroot, A. Martinez, and R. Beemer. “Uplift resistance of a multiline ring anchor system in soft clay to extreme conditions.” In *Geo-Extreme 2021*, pp. 413-424. 2021.

Lee, J., M. Khan, L. Bello, and C. P. Aubeny. “Cost analysis of multiline ring anchor systems for offshore wind farm.” In *Proc., Deep Foundation Institute 45th Conference*, pp. 484-493. 2020.

© ASCE

Lee, J., S. Qin, K. Coughlan, and C. P. Aubeny. (2025, April). Decision-Making Framework for Marine Anchor Selection in Floating Offshore Wind Farms. In *Offshore Technology Conference* (p. D021S106R003). OTC.

Locat, J., and D. Demers. (1988). "Viscous behaviour of clay and the interpretation of slope movements." *Canadian Geotechnical Journal*, 25(5), 799-806.

Lutenegger, A. J. (2011). "Helical Screw Anchors in Geotechnical Applications." *ASCE Geotechnical Special Publication*, 2, 1234-1245.

Mesri, G., and R. E. Olson. (1971). "Mechanisms controlling the permeability of clays." *Clays and Clay Minerals*, 19(3), 151-158.

Newmark, N. M. (1965). "Effects of earthquakes on dams and embankments," *Geotechnique*, 15(2), pp. 139-160.

Perko, H. (2009). *Helical Piles: A Practical Guide to Design and Installation*. John Wiley & Sons.

Qin, S., C. P. Aubeny, J. Lee, M. Alessandrini, L. Huang, and A. Martinez. (2025). "Load capacity of deeply embedded tubular anchor in normally consolidated clay under inclined loading." In *Proceedings of the 5th International Symposium on Frontiers in Offshore Geotechnics*. [forthcoming].

Qin, S., J. Lee, and C. P. Aubeny. (2024). Fatigue performance of the Deeply Embedded Ring Anchor. *International Journal of Geo-Engineering*, 15(1), 23.

Qin, S., J. Lee, and C. P. Aubeny. Evaluation of the Feasibility and Effectiveness of the Impact Hammer Installation of Deeply Embedded Ring Anchor. In *Geotechnical Frontiers 2025* (pp. 114-123).

Randolph, M., and S. Gourvenec. *Offshore geotechnical engineering*. CRC press, 2017.

Santamarina, J. C., A. Klein, and M. A. Fam. "Soils and waves: Particulate materials behavior, characterization and process monitoring." *Journal of Soils and Sediments* 1, no. 2 (2001): 130-130.

White, D. J., M. D. Bolton, and A. N. Schofield. (2002). "Soil Behavior in Vibratory Driving of Piles." *Journal of Geotechnical and Geoenvironmental Engineering*, 128(1), 66-77.

**© ASCE**

# Modeling Suction Bucket Foundations under Cyclic Loading through a Coupled Nonlocal Meshless Paradigm

Hossein Pashazad, S.M.ASCE[1]; and Xiaoyu Song, Ph.D., P.E., M.ASCE[2]

[1]Ph.D. Student, Dept. of Civil and Coastal Engineering, Univ. of Florida, Gainesville, FL.
Email: hossein.pashazad@ufl.edu
[2]Associate Professor, Dept. of Civil and Coastal Engineering, Univ. of Florida, Gainesville, FL.
Email: xysong@ufl.edu

## ABSTRACT

Suction bucket foundations are emerging as a promising alternative to traditional monopile foundations, particularly for offshore structures such as wind turbines, where stability under cyclic environmental loads is essential. This article investigates the loading capacity of suction buckets and the potential for soil liquefaction under static and cyclic loading conditions, utilizing an advanced nonlocal meshfree modeling approach called peridynamic poromechanics (PPM). The PPM paradigm is formulated by integral equations incorporating a length scale parameter, facilitating direct mechanical interactions between material points separated by finite distances. This nonlocal aspect allows the model to account for spatial dependencies in the soil's response, offering a robust solution to common limitations of traditional finite element models, such as mesh distortion and computational inefficiency under high-cycle loading. We implement the Norsand model through a return-mapping algorithm, which enables efficient numerical handling of complex soil behavior within this nonlocal context. Simulations of suction bucket foundations under static and dynamic loading provide insights into soil liquefaction potential and the foundation's load-bearing capacity. These findings underscore the effectiveness of the PPM approach combined with the Norsand model in predicting and managing long-term performance issues associated with suction bucket foundations, offering substantial potential for applications in offshore engineering where foundation stability is critical.

## INTRODUCTION

Suction buckets are a promising foundation solution for offshore wind energy systems (Achmus et al. 2013). Suction buckets appear similar to a gravity-based foundation but have long skirts around the perimeter. They are hybrid foundations taking design aspects from both shallow and pile foundation arrangements (Bye et al.2015). A caisson consists of a rigid circular lid with a thin tubular skirt of finite length extending below, giving it the appearance of a bucket. Two critical issues exist in the design of the bucket foundation: penetration of the skirts through the very dense sand and tension capacity, particularly under cyclic loading (Ding et al. 2015). The main topics considered for installing the bucket foundation are the touchdown of the skirts, the initial penetration of the skirts by structural weight, and suction-assisted penetration. The consolidation characteristics and the effects of soil dilatancy or contractancy are essential features of soil in the design analysis of bucket foundations (Ding et al. 2015). Most of the environmental loading applied to a bucket foundation is cyclic rather than monotonic (Wang et al. 2021). An additional fundamental mechanism contributing to the foundation response for such conditions is soil liquefaction due to pore pressure accumulation. Sands tend to generate

© ASCE

positive pore pressures during undrained cyclic loading as the soil matrix attempts to contract, i.e., increase in density (Wang et al. 2021).

Soil liquefaction has various detrimental effects, including foundation instability leading to structural damage or collapse, triggering landslides and slope failures. Norsand plastic material model has been implemented in the finite element method (FEM) for modeling soil liquefaction. However, the simulation of liquefaction through FEM may lose accuracy due to mesh distortion (Jefferies and Been 2015). The periporomechanics (PPM) paradigm handles this issue by incorporating the nonlocal length scale and using integral equations. In PPM, multiphase discontinuities emerge naturally from field equations and material models (Song and Silling, 2020). Incorporating classical constitutive models into the PPM framework is facilitated through the constitutive correspondence principle (Menon and Song, 2021a). The stabilized PPM correspondence principle (Menon and Song, 2021a, b) has been used to incorporate advanced classical constitutive models for the solid skeleton, and the stabilized multiphase PPM correspondence principle (Menon and Song, 2022a, b) enables the modeling of fluid flow using established fluid flow models, such as Darcy's law. A mathematical formulation for large-deformation PPM has been introduced within the updated Lagrangian-Eulerian framework, accompanied by a stabilization scheme based on energy methods (Menon and Song, 2023). Furthermore, the classical micropolar model has been integrated into the PPM framework to account for micro-rotation in granular materials, which studies its influence on strain localization and fracture behavior in porous media (Song and Pashazad, 2024; Pashazad and Song, 2024a, b, c).

In this article, the Norsand material model is incorporated within the multiphase PPM framework to simulate the suction bucket loading capacity and liquefaction of soil under cyclic loading. We have numerically implemented the novel PPM paradigm through an explicit algorithm at the global level and a return mapping algorithm for the Norsand material model at the local level. We validate our numerical model results by comparing the loading capacity with the FEM results. We also show the capability of the PPM paradigm in modeling the suction bucket foundation under cyclic loading.

## MATHEMATICAL FORMULATION

This part presents the governing equations of the unsaturated PPM paradigm for porous media and a bounding surface elastoplastic material model.

**Kinematics and governing equations.** A porous material body in PPM is represented by a collection of mixed material points. Each material point has two types of degrees of freedom, assuming atmospheric pore air pressure. By assuming a weightless pore air phase, the density of unsaturated porous media (Song and Silling 2020) is written as

$$\rho = \rho_s(1-\varphi) + S_r\varphi\rho_w, \tag{1}$$

where $\rho_s$ is the density of the solid phase, $\rho_w$ is the water density, $\varphi$ is the porosity, and $S_r$ is the degree of saturation. Through the effective state concept (Song and Silling 2020), the motion equation is written as

$$\rho^s \ddot{\boldsymbol{u}} = \int_{\mathcal{H}} \left( \underline{\overline{\boldsymbol{T}}} - \underline{\overline{\boldsymbol{T}}}' \right) dv' + \rho^s \boldsymbol{g}, \tag{2}$$

© ASCE

where $\rho^s = \rho_s(1-\varphi)$ is the partial density of the solid phase, $\boldsymbol{g}$ is the gravitational acceleration, $\underline{\overline{\boldsymbol{T}}}$ and $\underline{\overline{\boldsymbol{T}}}'$ are the effective force states, $\ddot{\boldsymbol{u}}$ is the acceleration, and $\mathcal{v}'$ is the volume of material point $\boldsymbol{x}'$. Assuming the passive air pressure, the effective force state $\underline{\overline{\boldsymbol{T}}}$ at material point $\boldsymbol{x}$ (Menon and Song 2021a) is written as

$$\underline{\overline{\boldsymbol{T}}} = \underline{\boldsymbol{T}} - \underline{\boldsymbol{T}}_{\boldsymbol{w}}, \tag{3}$$

where $\underline{\boldsymbol{T}}$ is the total force state and $\underline{\boldsymbol{T}}_{\boldsymbol{w}}$ is the fluid force state (Menon and Song 2021a). Assuming an incompressible solid phase, the mass balance equation of the mixture (Song and Silling 2020) is written as

$$\varphi\frac{dS_r}{dt} + \frac{\varphi S_r}{K_w}\frac{dp_w}{dt} + S_r\dot{V}_s + \frac{1}{K_w}\int_{\mathcal{H}}\left(\underline{\boldsymbol{Q}} - \underline{\boldsymbol{Q}}'\right)d\mathcal{v}' + Q_s = 0, \tag{4}$$

where $K_w$ is the bulk modulus of pore water, $\dot{V}_s$ is the solid volume change rate, $\underline{\boldsymbol{Q}}$ and $\underline{\boldsymbol{Q}}'$ are the fluid flow states, and $Q_s$ is a source term (Menon and Song 2022a). In the PPM framework, the bond between the material points located in $\boldsymbol{x}$ and $\boldsymbol{x}'$ in the initial configuration is defined as $\underline{\boldsymbol{\xi}} = \boldsymbol{x}' - \boldsymbol{x}$. The deformation state $\underline{\boldsymbol{Y}}$ is defined as

$$\underline{\boldsymbol{Y}} = \boldsymbol{y}' - \boldsymbol{y}, \tag{5}$$

where $\boldsymbol{y}'$ and $\boldsymbol{y}$ are the current location of material points $\boldsymbol{x}'$ and $\boldsymbol{x}$, respectively, in the deformed configuration. Given $\underline{\boldsymbol{Y}}$, the deformation gradient tensor in PPM (Menon and Song 2021a), is defined as

$$\boldsymbol{F} = \left[\int_{\mathcal{H}}\underline{\omega}\left(\underline{\boldsymbol{Y}}\otimes\underline{\boldsymbol{\xi}}\right)d\mathcal{v}'\right]N^{-1}, \tag{6}$$

where $\underline{\omega}$ is a weighting function, and $N$ is the shape tensor (Menon and Song 2021b). In the PPM framework, the time derivative of the deformation gradient tensor can be defined as

$$\dot{\boldsymbol{F}} = \left[\int_{\mathcal{H}}\underline{\omega}\left(\dot{\underline{\boldsymbol{Y}}}\otimes\underline{\boldsymbol{\xi}}\right)d\mathcal{v}'\right]N^{-1}. \tag{7}$$

From (6) and (7), the velocity gradient tensor is written as

$$\boldsymbol{L} = \boldsymbol{F}\dot{\boldsymbol{F}}^{-1}. \tag{8}$$

The rate of deformation tensor D reads

$$\boldsymbol{D} = \frac{1}{2}(\boldsymbol{L} + \boldsymbol{L}^{\boldsymbol{T}}). \tag{9}$$

The unrotated rate of deformation tensor $\boldsymbol{d}$ is written as

$$\boldsymbol{d} = \boldsymbol{R}\boldsymbol{D}\boldsymbol{R}^{\boldsymbol{T}}. \tag{10}$$

© ASCE

where $\boldsymbol{R}$ is the rotation tensor. Given the unrotated rate of deformation tensor, the strain increment can be obtained. The Piola stress tensor can be computed from a classical constitutive model. The force state in PPM can be written in terms of the Piola stress $\boldsymbol{P}$ as

$$\underline{\boldsymbol{T}} = \underline{\omega}\boldsymbol{P}N^{-1}\underline{\boldsymbol{\xi}}\,, \tag{11}$$

The Piola stress tensor can be obtained from the effective Cauchy stress $\boldsymbol{\sigma'}$ as

$$\boldsymbol{P} = J\boldsymbol{\sigma''}\boldsymbol{F^{-1}}\text{ , and }\boldsymbol{\sigma''} = \boldsymbol{R}\boldsymbol{\sigma'}\boldsymbol{R^{T}}, \tag{12}$$

where $J$ is the Jacobian. For the fluid phase, the fluid pressure state is defined as

$$\underline{\boldsymbol{\Phi}} = p'_w - p_w, \tag{13}$$

where $p'_w$ and $p_w$ are the fluid pressures at material points $\boldsymbol{x'}$ and $\boldsymbol{x}$, respectively. The water flow vector state $\underline{\boldsymbol{Q}}$ can be written as

$$\underline{\boldsymbol{Q}} = \underline{\omega}\boldsymbol{q_w}N^{-1}\underline{\boldsymbol{\xi}}\,, \tag{14}$$

where $\boldsymbol{q_w}$ is the fluid flux vector flux which can be obtained from Darcy's law as

$$\boldsymbol{q_w} = -\frac{k^r k_w}{\mu_w}\,\widetilde{\nabla\Phi}, \tag{15}$$

where $k_w$ is the intrinsic permeability, $k^r$ is the relative permeability, $\mu_w$ is the fluid viscosity and $\widetilde{\nabla\Phi}$ is the nonlocal fluid pressure gradient (Menon and Song 2021a). In the PPM framework, the fluid pressure gradient is written as

$$\widetilde{\nabla\Phi} = \left(\int_{\mathcal{H}} \underline{\omega}\underline{\boldsymbol{\Phi}}\,\underline{\boldsymbol{\xi}}\,d\mathcal{V}'\right)N^{-1}, \tag{16}$$

**Stress-strain relation.** For a loading process inside the bounding surface, elastic and plastic strains occur. Following a small-strain assumption, the additive decomposition of strain $\boldsymbol{\varepsilon}$ into elastic and plastic parts is written as

$$\boldsymbol{\varepsilon} = \boldsymbol{\varepsilon^{e}} + \boldsymbol{\varepsilon^{p}}\,, \tag{17}$$

where $\boldsymbol{\varepsilon^{e}}$ is the elastic strain tensor and $\boldsymbol{\varepsilon^{p}}$ is the plastic strain tensor. The elastic volume strain and equivalent shear strain can be defined as

$$\varepsilon_v^e = \text{tr}(\boldsymbol{\varepsilon^{e}})\text{ , and }\varepsilon_q^e = \sqrt{\frac{2}{3}}||\boldsymbol{\varepsilon^{e}} - \frac{1}{3}\varepsilon_v^e\mathbf{1}||, \tag{18}$$

where $\mathbf{1}$ is the second-order identity matrix, $\varepsilon_v^e$ is the elastic volume strain and $\varepsilon_q^e$ is the equivalent elastic shear strain. The effective mean stress $p'$ and the equivalent shear stress q are respectively obtained by

© ASCE

$$p' = K\boldsymbol{\varepsilon}_{\boldsymbol{v}}^{\boldsymbol{e}}\text{, and } q = \mu\varepsilon_q^e, \tag{19}$$

where $K$ is the bulk modulus and $\mu$ is the shear modulus. The relation among the effective stress, effective mean stress, and the equivalent shear stress can be written as

$$\boldsymbol{\sigma}' = p'\mathbf{1} + \sqrt{\frac{2}{3}}\mathrm{q}\mathbf{n}\text{, and } \mathbf{n} = \frac{\boldsymbol{\sigma}' - p'\mathbf{1}}{||\boldsymbol{\sigma}' - p'\mathbf{1}||}. \tag{20}$$

**Norsand plasticity.** In the Norsand plasticity model, a yield surface is used to describe the elastoplastic behavior of sand. The yield surface (Jefferies 1993) is written as

$$\mathrm{f} = q + \eta p', \tag{21}$$

where

$$\eta = M[1 + \ln(\frac{p_i}{p'})], \tag{22}$$

where $p_i$ is the image stress on the representing the size of the yield surface, M is the slope of the critical state line. The image stress can be presented as

$$p_i = \exp(\frac{\eta}{M} - 1), \tag{23}$$

For the non-associated plasticity, the plastic potential can be defined as

$$\mathrm{Q} = q + \overline{\eta} p', \tag{24}$$

where

$$\overline{\eta} = M[1 + \ln(\frac{\overline{p_i}}{p'})], \tag{25}$$

and $\overline{p_i}$ can be presented as

$$\overline{p_i} = \exp(\frac{\overline{\eta}}{M} - 1). \tag{26}$$

For the plastic potential, if $\overline{p_i} = p_i$, one will have the associative plasticity.

First, we define the state parameter to present the hardening law. The state parameter $\Psi = e - e_c$ is defined as the difference between the current void ratio $e$ and the critical state void ratio $e_c$ (Jefferies 1993). Plastic dilatancy, which allows a softening response in the plastic model, is defined as the ratio between the volumetric and deviatoric components of plastic strain rates (Jefferies and Been 2015) as

$$D^p = \frac{\dot{\varepsilon}_v^p}{\dot{\varepsilon}_q^p} = M - \eta, \tag{27}$$

© ASCE

where $\bar{\eta}$ is the ratio of image stress. The maximum plastic dilatancy $D^p_{max}$ can be determined by the following empirical correlation (Jefferies 1993) as

$$D^p_{max} = \alpha\Psi_i \text{ , and } \Psi_i = \Psi + \lambda \ln\left(\frac{p_i}{p'}\right), \tag{28}$$

where α is the material constant, and $\overline{p}_i$ is the image pressure (Jefferies 1993). The image pressure in the rate form is written as

$$\dot{p}_i = h(p_{i,max} - p_i)\, \dot{\varepsilon}^p_q, \text{ and } p_{i,max} = p'\left(-\frac{\alpha\Psi_i}{M}\right), \tag{29}$$

where h is the hardening parameter (Jefferies 1993). The plastic flow rule for the volumetric and equivalent shear strain is written as

$$\dot{\varepsilon}^p_v = \dot{\gamma}\frac{\partial Q}{\partial \boldsymbol{\sigma}'}, \tag{30}$$

where $\dot{\gamma}$ is the plastic. From the condition of consistency, the plastic hardening modulus is written as

$$H^p = M(\frac{p_i}{p'})h(p_{i,max} - p_i)\,. \tag{31}$$

To solve the governing equations, a hybrid Lagrangian-Eulerian meshless scheme was applied in the spatial domain and an explicit-explicit dual-direction fractional-step algorithm was used in the temporal domain. The porous material body is discretized into a finite number of mixed material points. The solid phase is tracked using a Lagrangian coordinate, which represents the material's deformation, while the fluid phase is tracked using an Eulerian coordinate relative to the solid phase (Pashazad and Song 2024a; Menon and Song 2022b). Moreover, the return mapping algorithm was used to implement the Nor-sand material model.

## NUMERICAL EXAMPLES

In this section, the numerical examples are presented to show the efficacy and accuracy of the implemented PPM paradigm in modeling the bearing capacity of suction bucket foundations and soil liquefaction around such foundations.

**Suction bucket under a monotonic vertical load.** In this example, we show the efficacy of the proposed PPM paradigm for the suction bucket loading capacity. Figure 1 shows the geometry, boundary conditions, and the water table adopted in this example. The base is constrained against vertical motion, and the horizontal ends are constrained against lateral movement. In this example we compare the PPM results with the FEM results (PLAXIS 3D). The problem domain is discretized into 54,240 uniform mixed points with a grid size of 0.05 m. The horizon is 0.15 m. In this example, the material is considered a single, slightly overconsolidated sand. The input material parameters adopted are bulk modulus K=45 MPa and shear modulus μ=25 MPa, the initial porosity 0.3, the critical state line M=1.1, swelling/recompression index λ=0.085, α=3.5, h=65 and initial state parameter 0. The Norsand material model for PLAXIS 3D is adopted with the same material parameters.

© ASCE

Next, we compare our numerical results with those of the FEM results. Figure 2 plots the loading curve from PPM and FEM simulations. As implied from the results, the loading capacity from PPM simulation agrees with the FEM result. Figure 3 compares the contours of displacement magnitude, equivalent shear strain, pore pressure, and volumetric strain at the loading 2 mm from FEM and PPM simulations. As shown in the results, the general trend of our numerical results agrees with the FEM results.

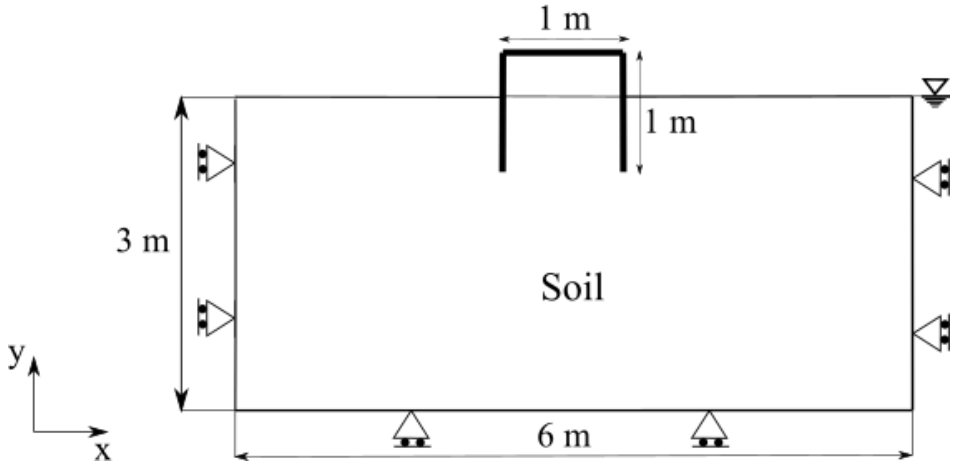



**Figure 1. Model setup for the loading capacity of a suction bucket.**

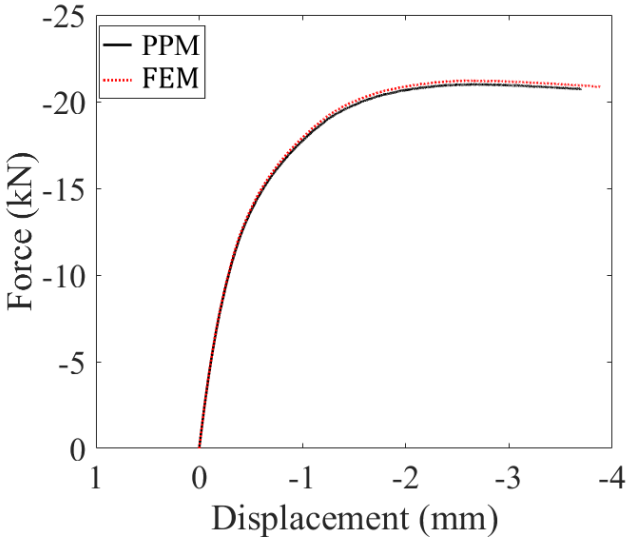



**Figure 2. Comparison of loading capacity from FEM and PPM simulation.**

**Suction bucket under cyclic loads**. In this example, we show the capability of the proposed PPM paradigm for suction bucket under cyclic loading. Figure 4 shows the geometry, water table, and boundary conditions adopted in this example. The cyclic horizontal displacement is imposed between 6 mm to -6 mm. The base is constrained against vertical motion, and the horizontal ends are constrained against lateral movement. In this example, we consider three initial state parameters, i.e., 0.04, 0, and -0.04. The remaining material parameters are the same

© ASCE

as the first example. The problem domain is discretized into 27,140 uniform mixed points with a grid size of 0.1 m. The horizon is 0.2 m, and the stable critical time is 0.01 s.

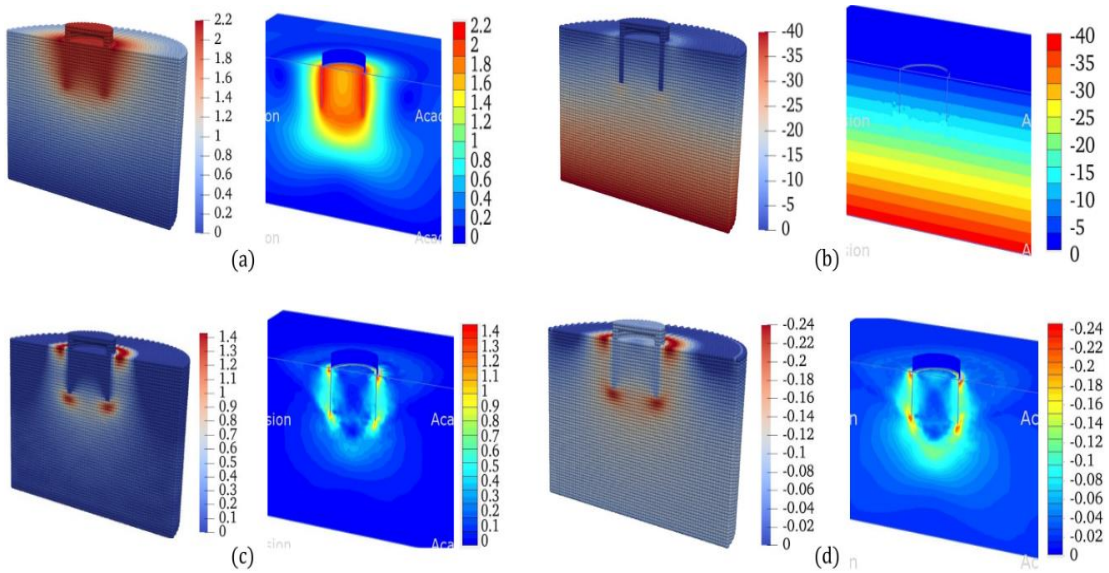



**Figure 3. Contours of (a) displacement magnitude (mm), (b) pore pressure (kPa) (c) equivalent shear strain (%), and (d) volume strain (%) from PPM (left) and FEM (right).**

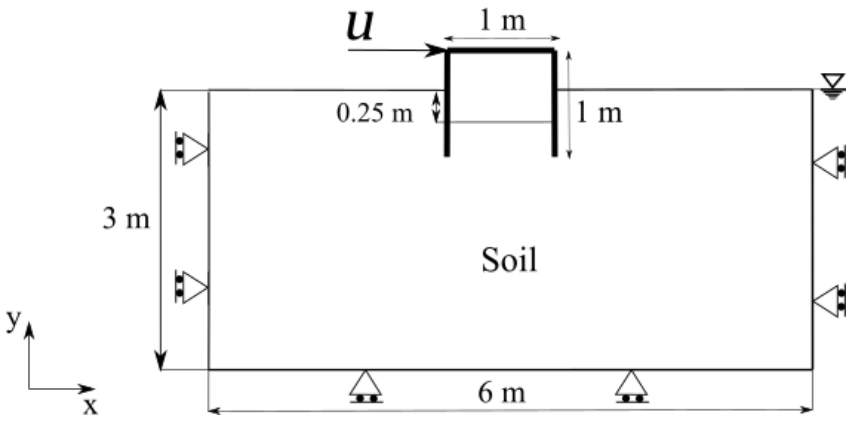



**Figure 4. Model setup for suction bucket under cyclic loading.**

The numerical results are presented in Figure 5. The first row of Figure 5 shows the snapshots of displacement in a deformed configuration at the same loading stage for the three cases. The second row of Figure 5 plots the equivalent plastic shear strain snapshots at three loading stages. The third row of Figure 5 presents the snapshots of water pressure in a deformed configuration at the same loading stages. The results in Figure 5 demonstrate that the largest deformation and plastic strain occurred in the looser sand with state parameter -0.04 around the suction bucket foundation, and the increasing water pressure occurred in the plastic zone. The latter may imply that liquefaction happens around the suction bucket foundation.

© ASCE

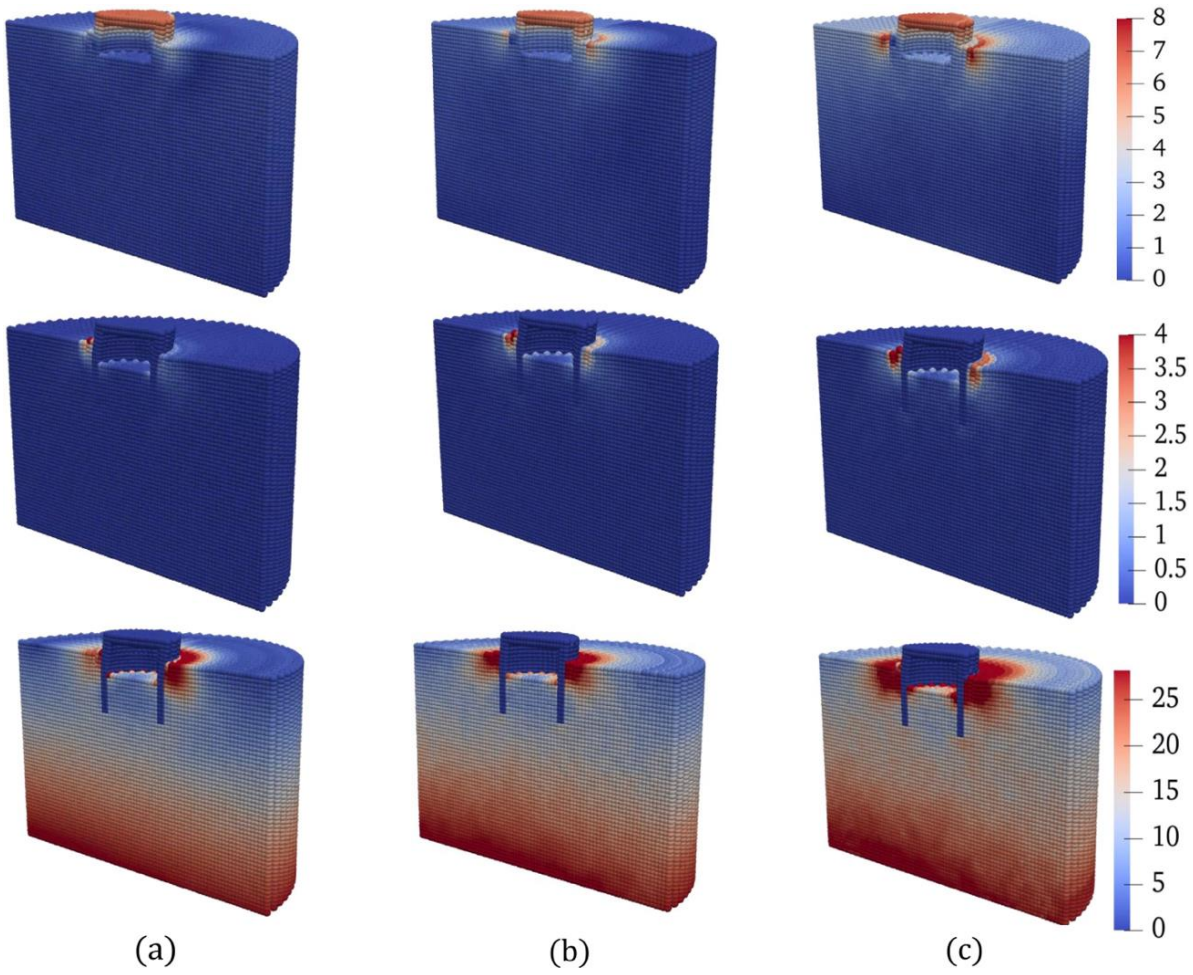



**Figure 5. Contours of displacement magnitude (mm) (top row), equivalent plastic shear strain (%) (2nd row), and pore pressure (kPa) (3rd row) at loading u=6 mm of second cycle for the state parameter (a) 0.04, (b) 0 and (c) -0.04.**

## CONCLUSION

In this article, we have implemented the Norsand material model into a multiphase PPM paradigm for modeling liquefaction in porous media. We have numerically implemented the novel PPM paradigm through an explicit algorithm at the global level and a return mapping algorithm for the Norsand material model at the local level. Numerical examples are presented to evaluate the numerical implementation and demonstrate the efficacy of the proposed PPM paradigm for modeling the bearing capacity of suction bucket foundation and pore water pressure buildup around the suction bucket foundation under cyclic loading.

## ACKNOWLEDGEMENTS

This work was partially supported by the US National Science Foundation CAREER program under contract number CMMI 1944009.

© ASCE

## REFERENCES

Achmus, M., Akdag, C. T., and Thieken, K. “Load-bearing behavior of suction bucket foundations in sand.” *Applied Ocean Research* 43 (2013): 157-165.

Bye, A., Erbrich, C., Rognlien, B., and Tjelta, T. I. “Geotechnical design of bucket foundations.” In *Offshore Technology Conference*, pp. OTC-7793. OTC, 1995.

Ding, H., Liu, Y., Zhang, P., and Le, C. “Model tests on the bearing capacity of wide-shallow composite bucket foundations for offshore wind turbines in clay.” *Ocean Engineering* 103 (2015): 114-122.

Jefferies, M., and Been, K. (2015). *Soil liquefaction: a critical state approach*. CRC Press.

Jefferies, M. G. (1993). “Nor-Sand: a simple critical state model for sand.” *Géotechnique.* 43(1). 91-103.

Menon, S., and Song, X. (2021a). “A computational peripоromechanics model for localized failure in unsaturated porous media.” *Comput Methods Appl Mech Eng.* 384. 113932.

Menon, S., and Song, X. (2021b). “A stabilized computational nonlocal poromechanics model for dynamic analysis of saturated porous media.” *Int J Numer Methods Eng.* 122, 5512–39.

Menon, S., and Song, X. (2022a). “Computational multiphase peripоromechanics for un-guided cracking in unsaturated porous media.” *Int J Numer Methods Eng.* 123, 2837–71.

Menon, S., and Song, X. (2022b). “Updated Lagrangian unsaturated peripоromechanics for extreme large deformation in unsaturated porous media.”, *Comput Methods Appl Mech Eng.* 400, 115511.

Pashazad, H., and Song, X. (2024a). “Computational multiphase micro-peripоromechanics for dynamic shear banding and fracturing of unsaturated porous media.” *Int J Numer Methods Eng.*, 125, e7418.

Pashazad, H., and Song, X. (2024b). “Modeling dynamic crack branching in unsaturated porous media through multiphase micro-peripоromechanics.” *Int. J. Numer. Anal. Methods Geomech.*,

Pashazad, H., and Song, X. (2024c). “Shear banding and cracking in unsaturated porous media through a nonlocal THM meshfree paradigm.” *Geosciences.*, 14(4), 103.

Song, X., and Pashazad, H. (2024). “Computational Cosserat peripоromechanics for strain localization and cracking in deformable porous media.” *Int. J. Solids Struct.*, 288, 112593.

Song, X., and Silling, S. A. (2020). “On the peridynamic effective force state and multiphase constitutive correspondence principle. *J. Mech. Phys. Solids*, 145, 104161.

Wang, J., Sun, G., Chen, G., and Yang, X. “Finite element analyses of improved lateral performance of monopile when combined with bucket foundation for offshore wind turbines.” *Applied Ocean Research* 111 (2021): 102647.

© ASCE

# Finite Element Modeling of Soil-Foundation-Structure Interaction for Seismic Performance of Nuclear Power Plants

Lei Wang, M.ASCE[1]; and Skarleth Gutierrez, S.M.ASCE[2]

[1]Assistant Professor, Dept. of Civil and Architectural Engineering and Construction Management, Univ. of Cincinnati, Cincinnati, OH. Email: wang4li@ucmail.uc.edu
[2]Research Assistant, Dept. of Civil and Architectural Engineering and Construction Management, Univ. of Cincinnati, Cincinnati, OH. Email: gutiersd@mail.uc.edu

## ABSTRACT

Nuclear power plants (NPPs) are critical components of the national energy infrastructure and must operate safely and reliably under seismic conditions. The interactions between the soil, foundation, and structure play a pivotal role in the dynamic response of the nuclear infrastructure system under earthquakes. In this study, an advanced three-dimensional soil-foundation-structure model is developed using the 3D finite element modeling, comprehensively accounting for the nonlinear dynamic behavior of the soil, the elastoplastic characteristics of the foundation, and the vibrational response of the structure. This paper investigates the seismic mitigation performance of a periodic foundation by evaluating the effects of two different raft foundations on structural responses of the nuclear power plant under seismic wave inputs. The results demonstrate the performance of periodic foundations to mitigate seismic impacts, thereby providing the theoretical basis for optimizing seismic design and the practical implementation of 3D base isolation in nuclear power plants.

## INTRODUCTION

Nuclear power plants are a critical infrastructure for the efficient production of clean energy. However, their design requires utmost attention to safety, particularly in the face of natural disasters such as earthquakes, as structural damage to the nuclear reactor could result in severe radiation risks and environmental hazards. In the design of nuclear power plants, foundation seismic isolation technology is considered one of the effective measures for earthquake mitigation (Najafijozani et al. 2020; Zhu et al. 2022; Liu et al. 2024). Besides, some studies emphasized the differences in the dynamic behavior of structures built on soil compared to those with fixed foundations (Chopra and Gutierrez 1974; Coleman et al. 2016). The complex interactions among soil, foundation, and structure can significantly influence the overall dynamic response during seismic events (Bhaumik and Raychowdhury 2013; Gao et al. 2024). Furthermore, many seismic numerical studies of nuclear power plants overlook the nonlinear effects of the soil–foundation–structure system, such as the plastic deformation of soil, the nonlinear behavior of base isolation foundations, and the plastic damage of reinforced concrete structures (Kanellopoulos et al. 2024). Traditional seismic design methods often simplify or overlook these interactions, leading to a non-conservative design for nuclear power plants.

Reliable models that accurately replicate the seismic response of soil-foundation-structure interactions under intense earthquake ground motions are crucial for ensuring robust seismic design for nuclear power plants. To address the technical gap, a high-fidelity 3D finite element model of soil-foundation-structure interactions for nuclear power plants has been developed,

© ASCE

consisting of the soil, foundation, safety shell, and the surrounding auxiliary plant. The nonlinear soil-foundation interface and nonlinear soil response are incorporated to examine the role of each nonlinearity and to quantify its impact on soil-foundation-structure interactions and structural responses. Subsequently, the performance of periodic foundations in mitigating the seismic effects of nuclear power plants is comprehensively evaluated, with comparisons made against original foundations. This study conducts a comparative evaluation of seismic performance of two different raft foundations to provide valuable insights into the seismic design of nuclear power plants.

## SELECTION OF SEISMIC WAVES

In this study, a seismic ground motion record from the California earthquake is utilized to evaluate the effects of soil-foundation-structure interaction on the seismic response of nuclear power plants. The record was obtained by the U.S. Geological Survey using GEOS digital seismographs (Maley et al. 1989). Figure 1 shows the acceleration time history of seismic ground motion and its corresponding Fourier spectrum. The total duration of the motion has been adjusted to 20 seconds, with a scaling factor of 0.5. The peak ground acceleration of the input ground motion is -1.2g. While conducting the dynamic analysis, the ground motion input acceleration has been applied at the base of the raft foundation in *X*-directions.

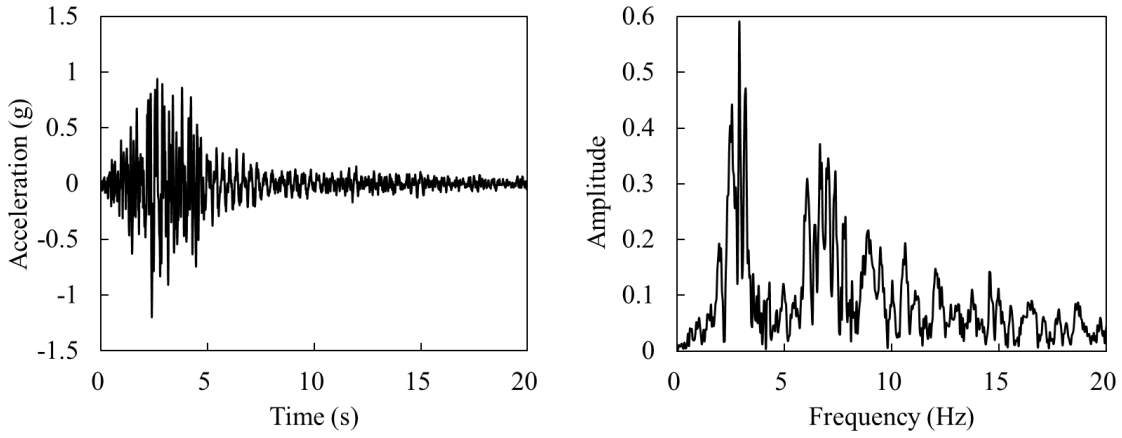



**Figure 1. The California earthquake ground motion and its Fourier spectrum**

## FINITE ELEMENT MODEL DEVELOPED BY PLAXIS 3D

A three-dimensional finite element model of the nuclear power plant is built consisting of three parts: a safety shell, an auxiliary plant, and a raft foundation, as shown in Figure 2. The safety shell has a total height of 73 m and a radius of 21.5 m, with wall thickness of 1.5 m. It is constructed of C60 concrete and simulated using solid elements. The auxiliary plant has floor heights of 5 m and 10 m, with 0.2 m thick C40 concrete walls simulated using plate elements. Designations R1-R3 and L1-L2 represent the reference points on the safety shell and the auxiliary plant respectively.

Two different raft foundation structures are constructed to compare their seismic mitigation performance: the original foundation and the layered periodic foundation. The original

© ASCE

foundation is composed of concrete with a thickness of 4 m, as shown in Figure 3 (a). The periodic foundation is composed of alternating layers of rubber and concrete materials, with the thickness of the concrete layer being 1 m and the thickness of the rubber layer being 0.2 m, as shown in Figure 3 (b). The concrete of the raft foundations is C40. The material properties adopted for modeling the safety shell, auxiliary plant, raft foundation, and soil are provided in Table 1, adapted from Sun et al. (2024). The hyperelastic properties of rubber are approximated using plate elements and an elastic model for analysis with Rayleigh damping values of 1273.44 for $\alpha$ and 0.03 for $\beta$ as referenced from Yusuf et al. (2018).

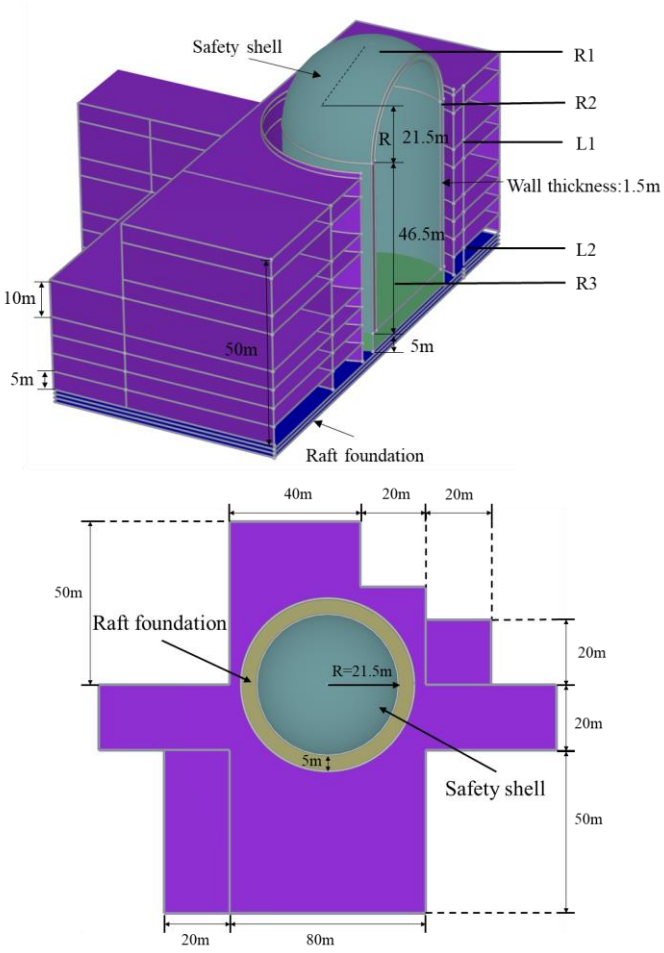



**Figure 2. 3D finite element model of the nuclear power plant**

Figure 4 shows the three-dimensional finite element model of the soil-foundation-structure system for the nuclear power plant. The length, width, and height of the soil model are 500, 500, and 80 m, respectively (Sun et al. 2024). In this study, the Mohr-Coulomb model is employed to simulate the nonlinear behavior of soil. The raft foundation of the nuclear power plant is tied to the model to ensure that the dynamic behaviors of the foundation and soil are synchronized under dynamic events. To simulate the radiation damping effect of an infinite medium on the near-field analysis region, a viscoelastic artificial boundary is applied to the truncated finite element model in a near-field wave finite element analysis. The soil at the boundaries is modeled

© ASCE

as infinite, with stress and displacement assumed to be zero at the computational domain boundaries to suppress the reverse propagation of waves within the domain. This approach also helps reduce redundant degrees of freedom and computational time (Islam et al. 2024).

**Table 1. Material properties adopted for finite element model**

| Materials for the model | Density (kg/m$^3$) | Young's modulus (Pa) | Poisson's ratio |
|---|---|---|---|
| C40 | 2400 | $3.25\times10^{10}$ | 0.2 |
| C60 | 2500 | $3.60\times10^{10}$ | 0.2 |
| Rubber | 1300 | $1.37\times10^{5}$ | 0.463 |
| Soil | 2400 | $4.00\times10^{10}$ | 0.394 |

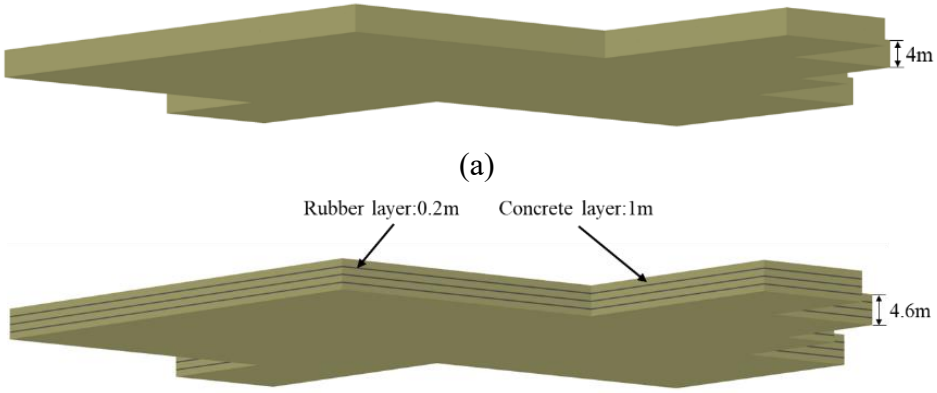



**Figure 3. Different raft foundation structures models: (a) Original foundation; (b)Periodic foundation**

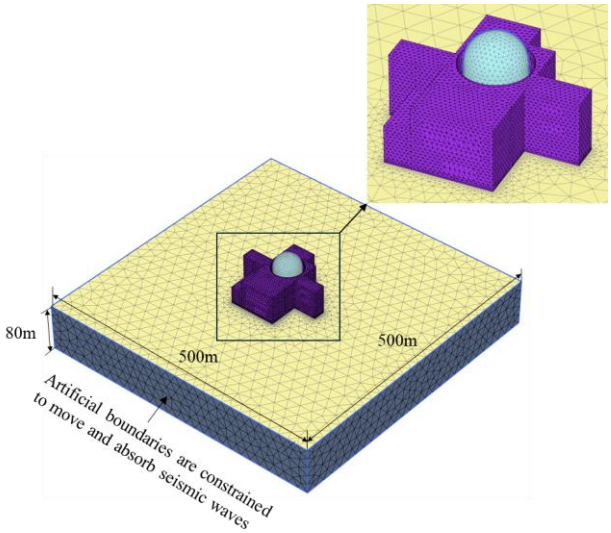



**Figure 4. Finite element mesh of soil-foundation-structure system**

© ASCE

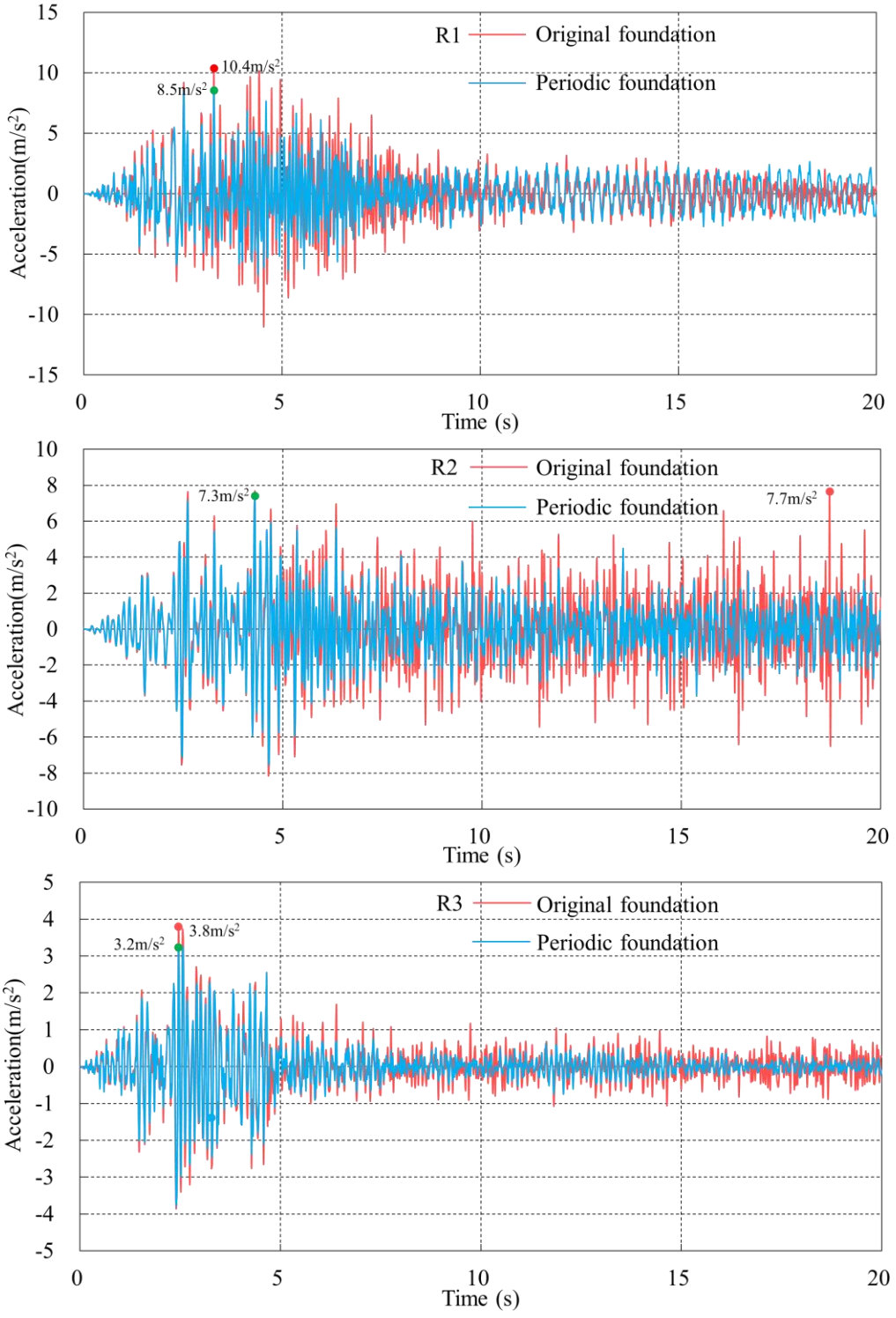



**Figure 5. Acceleration diagram of the nuclear power plant safety shell reference points under seismic motion**

This study investigates the seismic mitigation performance of a periodic foundation for nuclear power plants considering the soil–foundation–structure interaction. The time-history

© ASCE

analyses are evaluated by analyzing the acceleration of reference points, with Figures 5 and 6 presenting the acceleration time histories for the structure equipped with the original and periodic foundations, respectively. As shown, the peak acceleration of reference points on the safety shell increases with height from 5m (R3) to 73 m (R1). For the original foundation, the peak acceleration increases from 3.8 to 10.4 m/s$^2$, whereas for the periodic foundation, it rises from 3.2 to 8.5 m/s$^2$. This indicates a significant amplification of acceleration within the safety shell during seismic events, with the top of the safety shell posing a potential risk. Likewise, a similar trend is observed for the auxiliary plant, where the average acceleration of its reference points increases with height during seismic events. Through time-history analyses of various components of the nuclear power plant, its seismic performance and dynamic response characteristics can be thoroughly evaluated. The observed trend of increasing acceleration with height serves as a valuable reference for nuclear power plant design and the development of effective seismic protection.

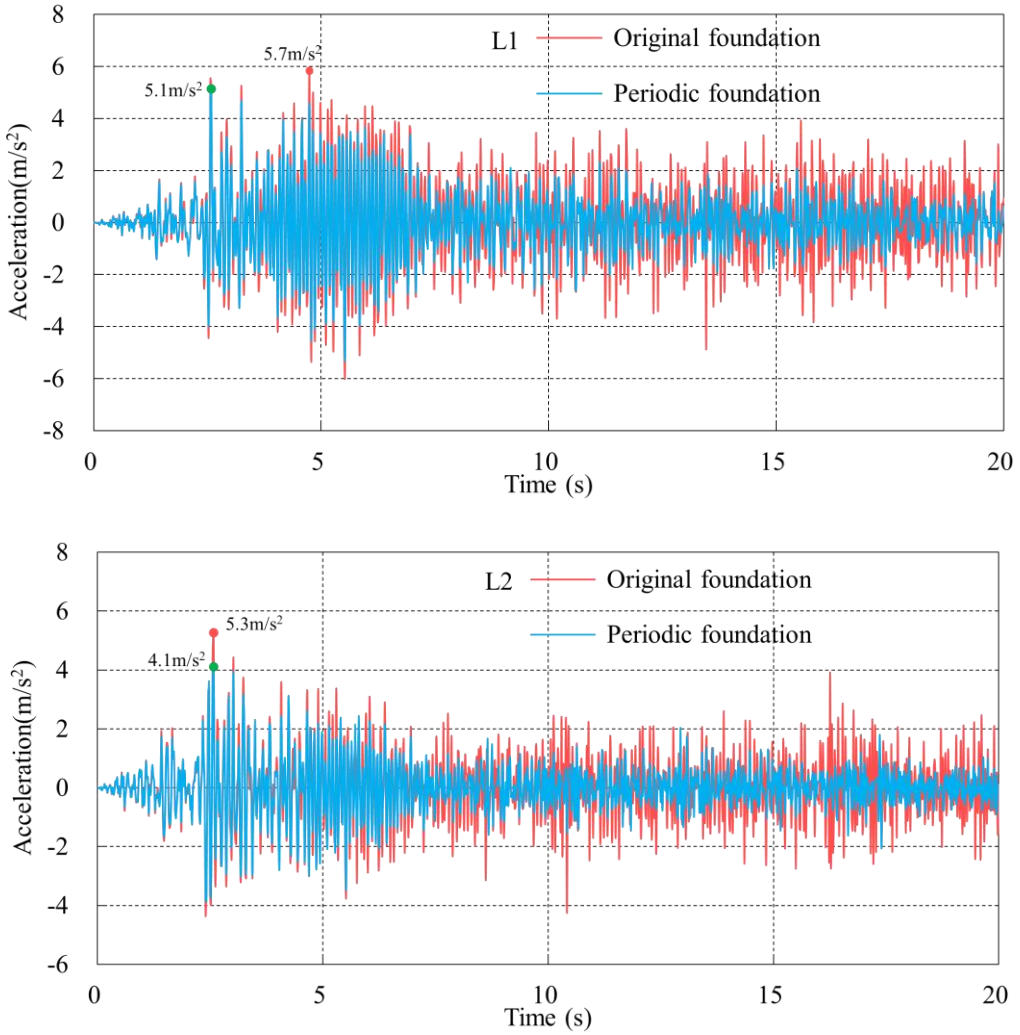



**Figure 6. Acceleration diagram of the nuclear power plant auxiliary plant reference points under seismic motion**

© ASCE

The nuclear power plant fitted with a periodic foundation exhibits substantially lower acceleration responses compared to the original foundation during seismic events. When replacing the original foundation with a periodic foundation, the peak acceleration at R1 decreases from 10.4 to 8.5 m/s², while at R2, it decreases from 3.8 to 3.2 m/s². The acceleration response at L1 and L2 indicates that the periodic foundation demonstrates significantly improved seismic performance for the auxiliary plant, particularly when subjected to high-frequency seismic inputs. The average acceleration response of the auxiliary plant built on the original foundation is significantly higher than that of one constructed with a periodic foundation, as shown in Figure 6. The results show that the seismic response of nuclear power plants can be significantly reduced by designing the periodic foundation.

## CONCLUSION

This paper presents a three-dimensional finite element modeling study to evaluate the effects of earthquake hazards on the system response of nuclear power plants. The analysis accounts for soil–foundation–structure interactions by defining the nonlinear characteristics of the soil, establishing tied interfaces between the soil and the foundation, and modeling the superstructure using solid elements. The results indicate an acceleration amplification effect within the nuclear power plant structure, placing the upper sections at significant risk of failure. The periodic foundation can effectively and significantly reduce the seismic response of the nuclear power plant. The seismic response patterns of the nuclear power plant structure and the demonstrated performance of the concrete-rubber periodic foundation offer valuable references for stakeholders regarding the seismic design and protection of nuclear power plants in the face of earthquake hazards.

## ACKNOWLEDGEMENTS

The study on which this paper is based was prepared under award 31310024M0040 from the Nuclear Regulatory Commission. The statements, findings, conclusions, and recommendations are those of the authors and do not necessarily reflect the view of the US Nuclear Regulatory Commission.

## REFERENCES

Bhaumik, L., and Raychowdhury, P. (2013). Seismic response analysis of a nuclear reactor structure considering nonlinear soil-structure interaction. *Nuclear Engineering and Design*, 265, 1078-1090.

Chopra, A. K., and Gutierrez, J. A. (1974). Earthquake response analysis of multistorey buildings including foundation interaction. *Earthquake Engineering and Structural Dynamics*, 3(1), 65-77.

Coleman, J. L., Bolisetti, C., and Whittaker, A. S. (2016). Time-domain soil-structure interaction analysis of nuclear facilities. *Nuclear Engineering and Design*, 298, 264-270.

Gao, L., Chen, S., and Sun, X. (2024). Two heterogeneous algorithms for partitioned analysis of nuclear power plants considering soil-structure interaction. *Nuclear Engineering and Technology*, 103393.

© ASCE

Islam, M. R., Turja, S. D., Van Nguyen, D., Forcellini, D., and Kim, D. (2024). Seismic soil-structure interaction in nuclear power plants: an extensive review. *Results in Engineering*, 102694.

Kanellopoulos, C., Rangelow, P., Jeremic, B., Anastasopoulos, I., and Stojadinovic, B. (2024). Dynamic structure-soil-structure interaction for nuclear power plants. *Soil Dynamics and Earthquake Engineering*, 181, 108631.

Kumar, S., Raychowdhury, P., and Gundlapalli, P. (2015). Response analysis of a nuclear containment structure with nonlinear soil–structure interaction under bi-directional ground motion. *International Journal of Advanced Structural Engineering (IJASE)*, 7, 211-221.

Liu, Y., Li, J., and Lin, G. (2024). Nonlinear numerical study of structure-soil-structure interaction effects between conventional and three-dimensional base-isolated nuclear power plants. *Soil Dynamics and Earthquake Engineering*, 187, 108985.

Maley, R., Acosta, A., Ellis, F., Etheredge, E., Foote, L., Johnson, D., Porcella, R., Salsman, M., and Switzer, J. (1989). U. S. Geological Survey strong-motion records from the northern California (Loma Prieta) earthquake of October 17, 1989, U. S. *Geological Survey Open-File Report* 89-568, 85 pages.

Najafijozani, M., Becker, T. C., and Konstantinidis, D. (2020). Evaluating adaptive vertical seismic isolation for equipment in nuclear power plants. *Nuclear Engineering and Design*, 358, 110399.

Sun, Z., Zhao, M., Gao, Z., Yao, D., Wu, L., and Du, X. (2024). Seismic mitigation performance of a periodic foundation for nuclear power structures considering soil-structure interactions. *Soil Dynamics and Earthquake Engineering*, 184, 108814.

Yusuf, A. I., Amin, N. M., Yunus, M. A., and Rani, M. N. A. (2018). Evaluation of Rayleigh Damping Coefficients for Laminated Rubber Bearing Components Using Finite Element and Experimental Modal Analysis. *International Journal of Integrated Engineering*, 10(9).

Zhu, X., Lin, G., Pan, R., and Li, J. (2022). Design and analysis of isolation effectiveness for three-dimensional base-seismic isolation of nuclear island building. *Nuclear Engineering and Technology*, 54(1), 374-385.

**© ASCE**

# Seismic Vulnerability Assessment of RC Buildings Considering Soil-Structure Interaction Effects with Mohr-Coulomb and Hardening Soil Models

Pranoy Debnath, S.M.ASCE[1]; Hamzah M. B. Al-Hashemi, A.M.ASCE[2]; and Deepankar Choudhury, F.ASCE[3]

[1]Postdoctoral Fellow, Dept. of Civil Engineering, Indian Institute of Technology Bombay, Powai, Mumbai, India. Email: pranoy.debnath9@gmail.com
[2]Ph.D. Research Scholar, Dept. of Civil Engineering, Indian Institute of Technology Bombay, Powai, Mumbai, India. Email: 23D0321@iitb.ac.in
[3]Professor T. Kant Chair Professor, Dept. of Civil Engineering, Indian Institute of Technology Bombay, Powai, Mumbai, India; Expert Member, High-Rise Committee of BMC, Mumbai, India. Email: dc@civil.iitb.ac.in

## ABSTRACT

Conventionally, reinforced concrete (RC) buildings are analyzed assuming a fixed foundation when assessing their seismic vulnerability. However, incorporating soil-structure interaction (SSI) into performance-based design approaches has gained global recognition in seismic engineering. The influence of SSI is particularly crucial for securing structures and those supported by deep foundations, where soil behavior significantly affects structural response. This study investigates the impact of SSI on the vulnerability and performance of RC moment-resisting frame (MRF) structures. Using a direct one-step modeling approach, site effects are integrated, considering both linear elastic and nonlinear soil behaviors. A five-story RC MRF is used as a reference structure. Based on the findings of the specified structural systems, the vulnerability of the structures is interpreted for the fixed-base and SSI models. The findings demonstrate that SSI effects are pivotal in modifying the expected structural performance and highlighting the necessity of accounting for soil behavior in seismic vulnerability assessments.

**KEYWORDS:** Soil-Structure Interaction; Reinforced concrete structures; Vertical loading; Lateral static pushover loading; Vulnerability.

## INTRODUCTION

In traditional structural dynamic analysis, it is commonly presumed to be rigid, thereby neglecting the elasticity of the soil (Debnath and Halder, 2019; Halder et al., 2021; Debnath et al., 2022, 2023a, 2023b; Debnath and Dutta, 2023, 2024). Under this assumption, the structural response is governed solely by its inherent dynamic properties, without any influence from soil flexibility. This holds true when buildings are constructed on rock formations; however, their response deviates significantly in several cases where structures are founded on soft soil. In such scenarios, the interaction effects between soil and structure alters foundational movements, leading to a mutual exchange of forces-commonly referred to soil-structure interaction (Saha et al., 2020; Hamidia et al., 2021; Chanda et al., 2023; Das et al., 2023, 2025; IS 19117, 2025). This interaction considerably impacts the overall structural response. The study of soil dynamics initially started by Lamb (Lamb, 1904), who first examined elastic vibrations, laying the groundwork for research in this field. Building upon Lamb's work, Reissner (1936) investigated

© ASCE

vibrations of circular rigid foundations on elastic soil, marking the early exploration of soil-structure interaction (Reissner, 1936). In subsequent research, Hokmabadi et al. (2014) examined the soil-pile-structure interaction (SPSI) case and its impact on the dynamic behavior of buildings, revealing that seismic SPSI leads to amplified lateral deflections and interstory drifts in structures supported by end-bearing pile foundations compared to fixed-base buildings (Hokmabadi et al., 2014). Furthermore, Fatahi et al. (2014) explored the behavior of pile foundations under lateral loads, noting that in soft clay, lateral forces can cause soil heave, tension cracks, and gap formation around the pile-soil interface (Fatahi et al., 2014). These findings highlight the significance of incorporating soil-structure interaction in structural design to enhance the accuracy of dynamic response predictions.

Soil-structure interaction (SSI) analysis is broadly categorized into direct method and the multistep method. The direct approach involves analyzing the entire structure-foundation-soil system simultaneously within a single computational framework, such as the finite element method (FEM). One of the key advantages of this approach is its ability to incorporate nonlinear material behavior for both soil and structural elements, while also accommodating complex geometries (Wolf, 1985). Proper modeling of the soil-structure system is essential considering the significance of soil-structure interaction in both geotechnical and structural engineering. Accurate numerical modeling tools that integrate both geotechnical and structural analysis capabilities are crucial for reliable assessments. Recently, several studies have examined how soil-structure interaction (SSI) influences the seismic behavior of structures (Katzenbach et al., 2016; Bolisetti and Whittaker, 2020; Patil et al., 2023; Fatahi and Tabatabaiefar, 2024) and some other studies also developed fragility curves for RC buildings considering the SSI effects (Sáez et al., 2011; Tahghighi and Mohammadi, 2020).

This study presents a comprehensive evaluation of SSI effect on five-storey mid-rise Reinforced Concrete (RC) structures under lateral and vertical loading conditions using finite element-based modeling in PLAXIS-3D. The novelty of the research is demonstrated through its innovative approach to SSI modeling, parametric investigations, and realistic soil-structure simulations. The study offers several contributions to the geotechnical and structural earthquake engineering field, differentiating itself by bridging the gap between theoretical analysis and engineering practice. The research provides valuable design insights that can be used in seismic retrofitting and earthquake-resistant construction.

## VALIDATION FOR THIS STUDY

## SOIL MODEL VALIDATION

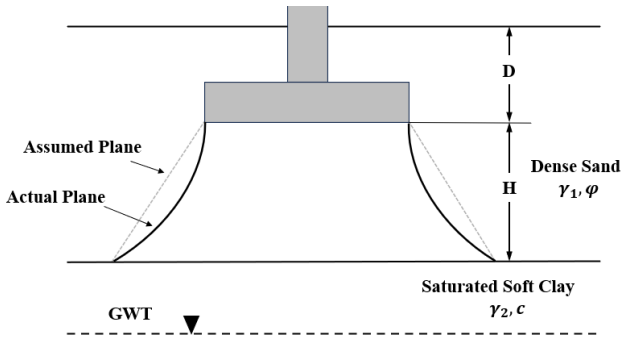
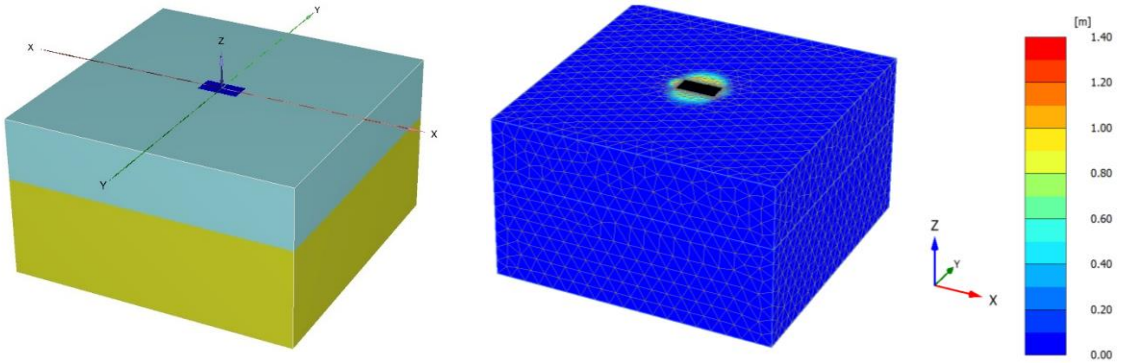



**Figure 1. Schematic diagram of footing system in layered deposit.**

© ASCE




(a) (b)

**Figure 2. Square/Rectangular footing (a) model embedded in layered deposit and (b) vertical settlement pattern.**

The schematic diagram of a rectangular footing is shown in Figure 1. The footing has dimensions L, width B, and depth D, and is sited in a dense sand layer that rests above a saturated soft clay layer. The vertical distance from footing base to the interface between thick sand and soft clay is represented by H. The soil parameters for saturated soft clay and dense sand are represented by $\gamma_2, c$ and $\gamma_1, \varphi$ respectively. The unit weight of the upper stratum is equal to 14.95 kN/m$^3$ and the undrained shear strength is equal to 9.85 kN/m$^2$ is considered for rectangular footing of length to width ratio 2. The load applied to the footing is considered to spread out at an angle from its base, covering an increasingly larger area of the sand layer as it moves deeper into the soil layer. Consequently, load intensity also reduces with depth, forming a frustum-shaped failure zone, which serves as a simplified representation of the actual failure surface. This model has been implemented in Plaxis 3D to accurately simulate the bearing behavior and failure mechanism, as depicted in Figure 2.

Results are presented in Eq. (1) for normalized ultimate bearing capacity variation with corresponding normalized cohesive strength of clay $\frac{c}{(\gamma_1 B)}$. The other variables are thickness ratio $\left(\frac{H}{B}\right)$, dispersion angle of the load ($\alpha$) and length to width ratio ($\frac{L}{B}$) considering rectangular footing (Gupta et al., 2011).

$$\frac{q_u}{\gamma_1 B} = \frac{\left(1+0.2\frac{B}{L}\right)cN_c}{\gamma_1 B} + \frac{D}{B} + \frac{K_p' 2\left(D+\frac{H}{2}\right)H \sin\delta\left(1+\frac{L}{B}+\frac{H}{B}4\tan\alpha\right)}{LB+2H\tan\alpha(L+B)+4H^2 tan^2\alpha} \quad (1)$$

Where, Friction angle of the soil ($\varphi$) = 25°, 30°, 35°, and 40°
Normalized cohesive strength of clay = 0.5 and 1.0
Dispersion angle of the load is equal to 0°
Mobilised angle of shearing (δ) = $\varphi$ and 2 $\varphi$/3
Thickness ratio = 0.5 to 4.0 and Length to width ratio = 1.0 to 4.0 at an interval of 0.5.

A rectangular footing measuring 1.25 m by 2.5 m with a thickness of 0.3 m is placed on the sand layer of 3.818 m thickness for validation. The sand layer has a unit weight of 14.95 kN/m$^3$. Beneath this sand layer lies a saturated soft clay layer characterized by an undrained shear strength of 9.85 kN/m$^2$ (Dutta and Rao, 2008).

© ASCE

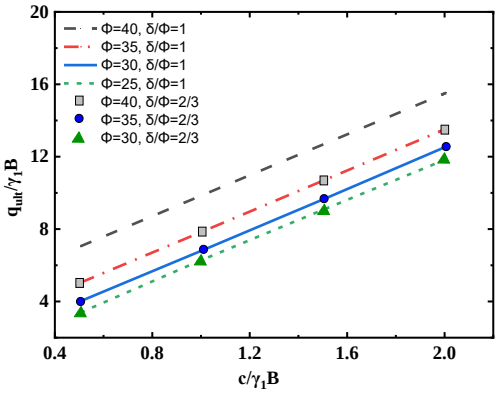



**Figure 3. Normalized ultimate bearing capacity variation curve with corresponding normalized cohesive strength of clay (length to width ratio = 2) when depth ratio = 0, thickness ratio = 0.5, and α = 0°.**

Figure 3 shows the effect of the normalized ultimate bearing capacity vs normalized cohesive strength of clay for rectangular footing from PLAXIS 3D analysis. The study indicates that as the normalized cohesive strength of clay rises from 0.5 to 2.0, there is a corresponding increase in the normalized ultimate bearing capacity. This trend aligns with the proposed equations, establishing a direct proportionality between these parameters. Additionally, an increase in undrained cohesive strength leads to overall improvement in bearing capacity of layered soil. These findings are consistent with previous research (Abdulhahz et al., 2005), which observed the behaviour of a stiff sand layer spread over the surface a soft clay layer.

## VALIDATION OF ONE-SPAN BEAM MODELING

To validate the analysis, a simply supported beam with a single span was modeled, subjected to two types of loading: a concentrated load at mid-span and a uniformly distributed load. Settlements and moment results were compared using classical structural analysis formulas. The beam's properties are detailed in Table 1.

**Table 1. Properties of Beam members for Modeling**

| Beam type | Size (cm) | Concrete Elastic modulus (E) (Pa) | Inertial moment (I) ($m^4$) | Moment of Resistance ($M_u$) (kNm) | Cross section A ($m^2$) | Length L (m) | Load | |
|---|---|---|---|---|---|---|---|---|
| | | | | | | | Concentrated (kN) | Distributed (kN/m) |
| Rectangular Concrete Beam | 35×45 | $2.5\times10^{10}$ | 0.0026578125 | 128.3 | 0.1575 | 4 | 10 | 5 |

The properties of both types of beams are shown in Table 1. The beams cannot function independently in PLAXIS software and require the soil for proper meshing. Initially, the soil analysis was disabled, allowing only the beams to be active. A separate region was defined to model the beams with various support conditions. Standard structural analysis equations were applied to determine the maximum settlement and moment, as presented in Equations (2) - (5).

© ASCE

$$\text{Maximum deflection with concentrated loading } \Delta_{max} = \frac{PL^3}{48EI} \quad (2)$$

$$\text{Maximum bending moment with concentrated loading } M_{max} = \frac{PL}{4} \quad (3)$$

$$\text{Maximum deflection with uniformly distributed loading } \Delta_{max} = \frac{5PL^4}{384EI} \quad (4)$$

$$\text{Maximum bending moment with uniformly distributed loading } M_{max} = \frac{PL^2}{8} \quad (5)$$

In these equations, $\Delta_{max}$ is maximum deflection of beam, $P$ donates concentrated load, and $M_{max}$ is maximum bending moment. A comparative analysis between the PLAXIS simulation results and the values derived from classical equations for maximum settlement and maximum bending moment in a simply supported beam under various loading conditions is presented in Table 2.

**Table 2. Comparison of the peak deflection and maximum moment for simply supported conditions obtained from Plaxis simulations and traditional structural analysis formulas**

| Support | Loading State | $\Delta_{max}$ (mm) | | $M_{max}$ (kN.m) | |
|---|---|---|---|---|---|
| | | Numerical | Analytical | Numerical | Analytical |
| Simple | Concentrated | 0.207 | 0.208 | 10.07 | 10 |
| Simple | Distributed | 0.250 | 0.251 | 10.07 | 10 |

Figure 4 presents the bending moment diagram (BMD) of a simply supported beam subjected to both concentrated and uniformly distributed loads. The numerical findings correspond well with the analytical calculations.

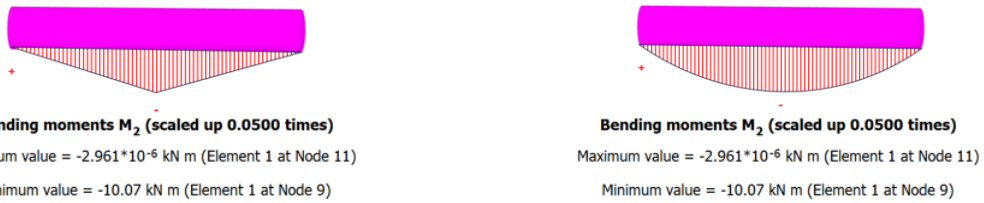
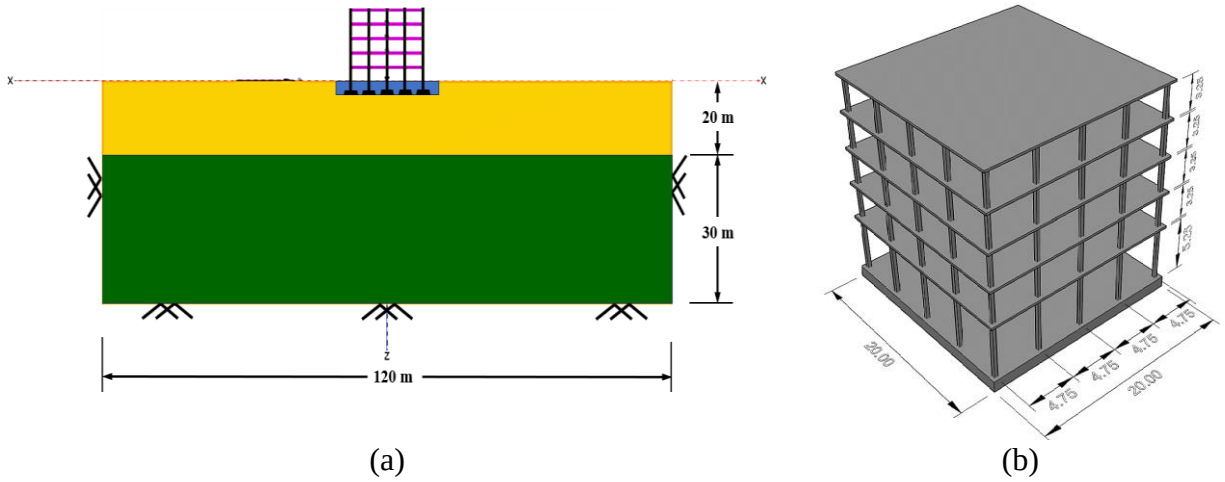



**Figure 4. Bending moment diagram of simply supported beam under (a) concentrated load and (b) uniformly distributed load.**

## DESCRIPTION OF THE PRESENT STUDY

Figure 5(a) shows the soil, foundation, and structural models used as references. Following earlier parametric research, the structural configuration models the cross-section of a typical reinforced concrete building consisting of four spans and four bays across five stories (Raj et al., 2024; Kiran et al., 2023). The bay widths and story heights are uniform throughout the structure, measuring 4.75 m and 3 m, respectively. This type of structural layout is commonly found in buildings globally, regardless of soil characteristics, as illustrated in Figure 5(b).

© ASCE




(a) (b)

**Figure 5. (a) Schematic diagram of soil-structural configurations and (b) schematic diagram of structural configurations (All dimensions are in meters).**

The proposed building configurations were established based on representative subsoil models, determined through parametric analyses (Raj et al., 2024). The mechanical characteristics of these subsoil models were selected to reflect realistic soil conditions, aligning, on average, with the Eurocode 8 (EC8) ground classification system (Eurocode 8, 2004), which is also commonly found in several Asian regions. The isolated foundations are embedded in a shallow soil cover, intensifying Soil-Foundation-Structure Interaction (SFSI) effects due to the relatively low stiffness contrast between the soil and the structure. A stiff bedrock layer, representative of ground type A, was uniformly assumed at a depth of 50 meters. In the stratified subsoil model, the shear stiffness of the D-type soil was matched to that of the homogeneous profile ($D_{ho}$), since stiffness variations within the top 5 meters are generally less impactful than those in deeper soil strata.

The numerical simulation for this study was conducted using finite element based PLAXIS-3D software. To represent the elastoplastic behavior of the soil, the Mohr-Coulomb model was employed, which was consistent with the approach used for validation. The mat foundation was represented as a plate element, incorporating a shallow foundation model with an interface element to account for soil-structure interaction. A linear skin resistance was applied at the plate-soil interface. A medium-mesh refinement was used for mesh generation, resulting in approximately 30,000 soil elements. Additionally, a very fine mesh refinement was tested to assess the accuracy of the results. Despite the longer computational time, the results showed minimal deviation compared to the medium mesh configuration. Therefore, the medium mesh refinement was deemed appropriate for this study. Standard boundary conditions were implemented, where the bottom boundary was fully constrained, and the vertical sides were restricted in the horizontal direction. The analysis was carried out in seven sequential phases, covering the initial setup, excavation, construction, and loading phases. Initially, the soil volume was introduced, followed by the deactivation of the soil above the isolated footing during the excavation phase. The footing and structural floors were sequentially activated during the construction phase, with self-weight effects incorporated into the analysis. The loading phase involved the application of an excitation force to assess the response. Finally, a pushover analysis was conducted on both the fixed base model and the model considering soil-structure interaction to evaluate their structural performance.

© ASCE

**Table 3. Parameters of soil**

| Sand Layer (top layer) | | Clay model (bottom layer) | |
|---|---|---|---|
| Properties | Soil model | Properties | Soil model |
| Model | Hardening soil model with small strain stiffness (HSS) | Model | Mohr-Coulomb |
| $\gamma_{unsaturated}$ | 17.8 kN/m$^3$ | Type | Undrained |
| $\gamma_{saturated}$ | 20.12 kN/m$^3$ | $\gamma_{unsaturated}$ | 17 kN/m$^3$ |
| $E_s$ | 42000 kN/m$^2$ | $\gamma_{saturated}$ | 18 kN/m$^3$ |
| $E_{ur}$ | 126000 kN/m$^2$ | $E_s$ | 50000 kN/m$^2$ |
| m | 0.481 | Cohesion (C) | 20 kN/m$^2$ |
| $P_{ref}$ | 60 kN/m$^2$ | Friction angle ($\varphi$) | $35^0$ |
| $G_0$ | 107600 kN/m$^2$ | ψ | $0^0$ |
| $Y_{0.7}$ | $1.3\times10^{-04}$ | Poisson's ratio (ν) | 0.35 |
| $R_f$ | 0.91 | | |
| *permability of sand* ($R_{int}$) | 0.67 | | |
| Friction angle ($\varphi$) | $35^0$ | | |
| ψ | $5^0$ | | |
| Poisson's ratio (ν) | 0.3 | | |

Tables 3 and 4 present the key soil characteristics and material properties for the isolated footing and slab. In the modeling process, both the soil and reinforced concrete were treated as continuum materials defined by their mass density (ρ), bulk modulus (K), shear modulus (G), and Poisson's ratio (ν). Floors and roofs were represented using equivalent beam elements composed of a homogenized material. The use of the modular ratio enabled the transformation of the composite section into an equivalent uniform section made of a single material (Kulkarni et al., 2014). The transformed section approach has certain limitations when used to locate the neutral axis by treating it as the centroid of the equivalent section. Stresses within the transformed section can be evaluated using the flexural formula, which requires the use of the second moment of area ($I_g$) of the transformed geometry. In this method, the area of tensile reinforcement ($A_{st}$) is converted into an equivalent concrete area by multiplying it with the modular ratio (m), resulting in m· $A_{st}$. This technique is applicable to reinforced concrete elements under bending and axial loads.

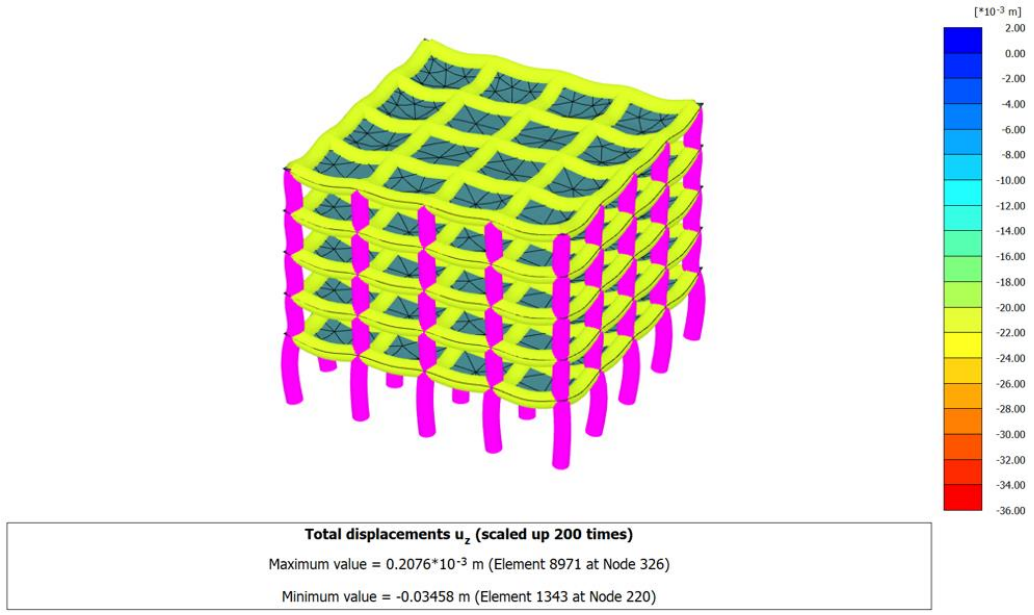
**Table 4. Parameters of raft footing and Slab**

| raft footing | | Slab | |
|---|---|---|---|
| Parameters | Values | Parameters | Values |
| Material Model | Elasto-plastic | Material Model | Elasto-plastic |
| Unit Weight | 21 kN/m$^3$ | Unit Weight | 24 kN/m$^3$ |
| Thickness, d (m) | 1.0 | Thickness, d (m) | 0.18 |
| Modulus of Elasticity (E) | 23.5 GPa | Modulus of Elasticity (E) | 23.5 GPa |
| Yield strength | 35 GPa | Yield strength | 35 GPa |
| Poisson's ratio (ν) | 0.2 | Poisson's ratio (ν) | 0.2 |

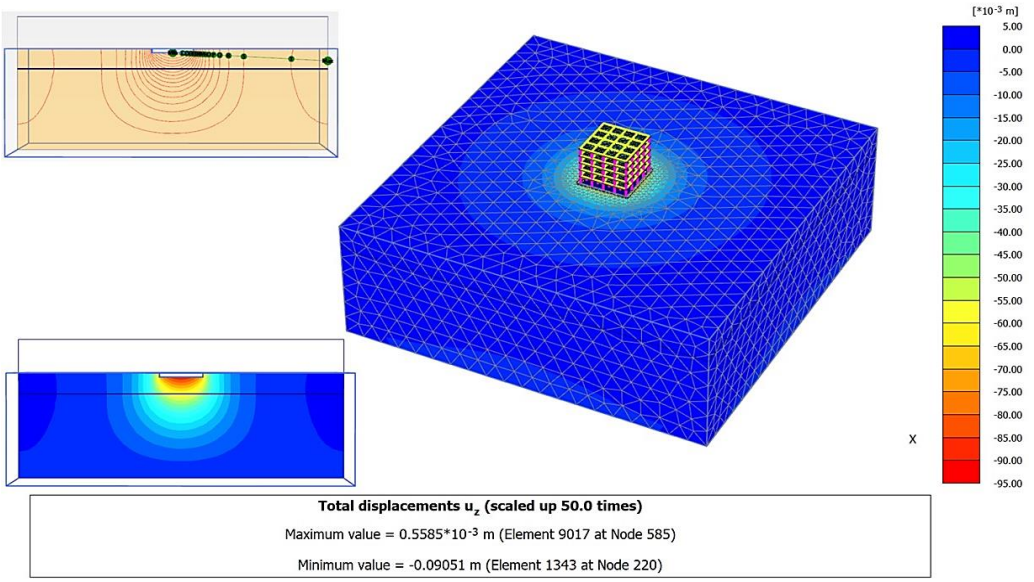
© ASCE

## RESULTS AND DISCUSSIONS

Compared with the fixed base condition, structures with a 50 m thick layer with the same soil configuration are also considered for checking the variation in results. Both vertical loads and horizontal static pushover conditions are checked for analysis. The maximum drift was compared as the engineering demand parameter.



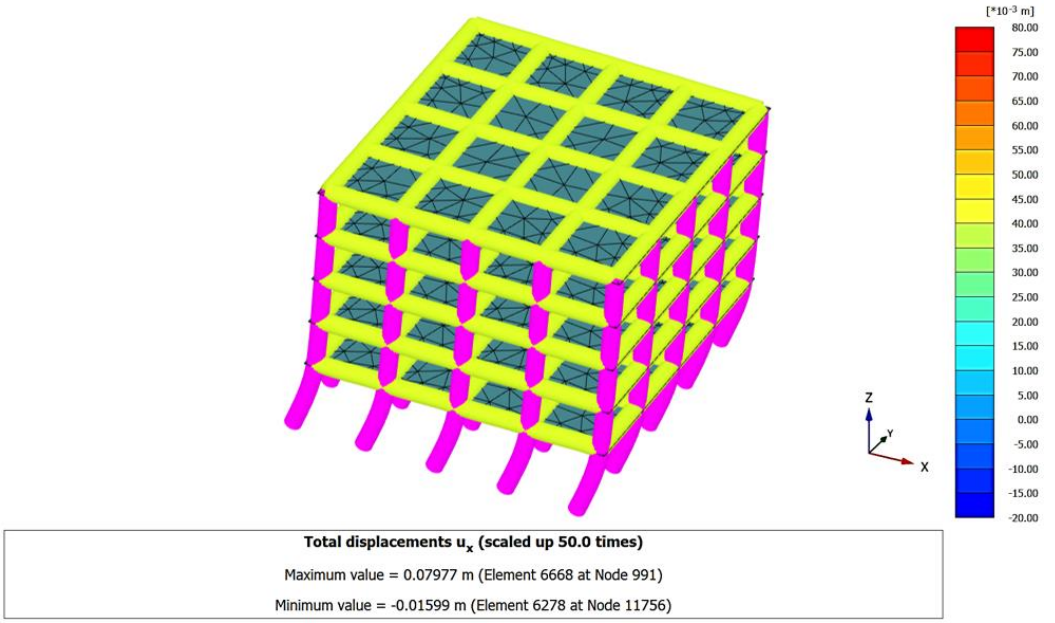

(a)



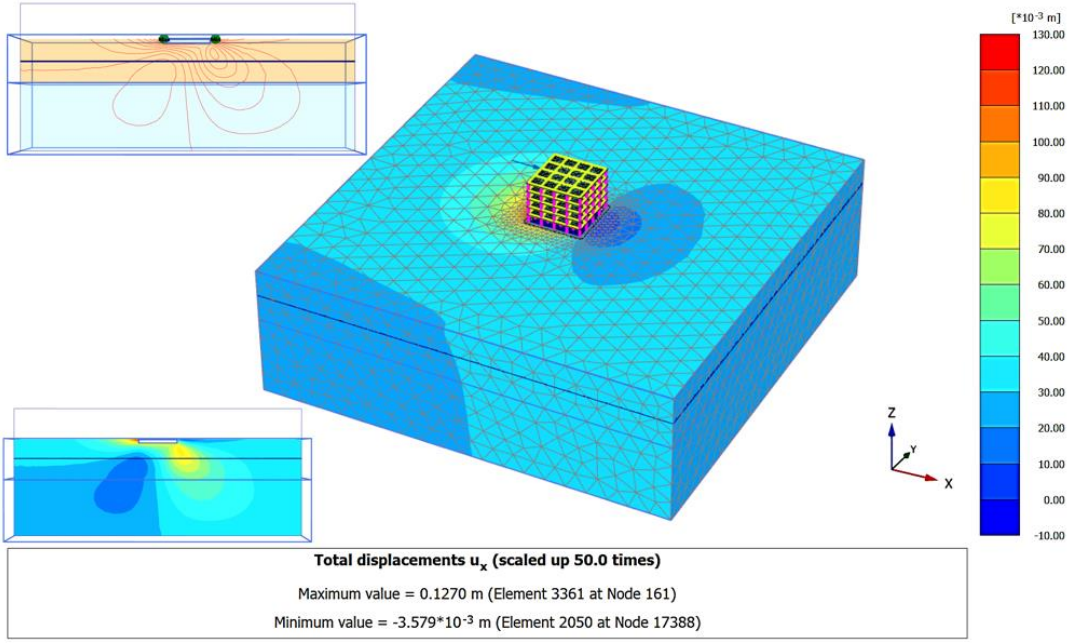

(b)

**Figure 6. Comparison of 5 storey building under vertical loading condition only (a) fixed base and (b) soil structure interaction case.**

© ASCE




(a)




(b)

**Figure 7. Comparison of 5-storey building under lateral static loading condition only (a) fixed-base and (b) soil-structure interaction case.**

## RESPONSE FOR VERTICAL LOADING CONDITION

Figure 6 compares the behaviour of a 5-storey building under vertical loading conditions. The building is assumed to have a rigid foundation in a fixed base case, meaning it does not experience settlements or deformations at the base. No deformation of the soil is considered, meaning that vertical loads (gravity, live loads) are entirely transferred to the foundation without

© ASCE

any settlement or rotation. Structural displacements and stresses are determined based only on the rigid base assumption. For the structure with soil-structure interaction (SSI) Case, the building is supported by a flexible soil foundation, which allows the foundation to interact with the underlying soil, causing soil deformation almost three times more than the fixed base case. The interaction of the superstructure with supporting soil affects the load distribution. The load transfer mechanism is affected, making the structural response more flexible than in the fixed base case. Increased bending moments and redistribution of internal forces may occur due to soil deformation. Slight tilting or increased stress concentrations can be observed in some columns. The fixed base assumption underestimates settlements under vertical loading.

## RESPONSE FOR HORIZONTAL STATIC PUSHOVER LOADING CONDITION

Figure 7 compares the same 5-Storey building under lateral static loading condition. The fixed-base case prevents any movement at the base. The building sways under lateral loading, but the foundation remains unaffected. Structural deformation is purely due to structural flexural and shear behaviour. For the soil-structure interaction (SSI) case, the foundation is flexible, meaning lateral loads cause both the building and the foundation to deform almost 1.5 times more than the fixed-base case. SSI influences the increased additional lateral drift at the top of the building due to the compliance of the supporting soil. The foundation tilting is due to soil flexibility, reduction in the overall stiffness of the structure, leading to more significant sway, and possibly increased bending moments and shear forces in structural elements. The fixed-base assumption underestimates lateral drift under lateral loading. SSI increases lateral deformations, potentially affecting seismic performance and structural stability.

## CONCLUSIONS

This study is one of the few research works that comprehensively integrates advanced SSI modeling, numerical validation, and vulnerability assessment in a single framework. By moving beyond traditional rigid base assumptions, the research sets a new benchmark for analysis methodologies for engineers, researchers, and policymakers. The findings can potentially improve the accuracy of earthquake-resistant designs, especially for structures built on soft or layered soils, thus making a significant contribution to geotechnical and structural earthquake engineering.

I. The study validated the PLAXIS 3D finite element software by comparing results with analytical solutions. Beam modeling tests showed close agreement between numerical and classical structural analysis solutions, confirming the accuracy of the software for SSI studies. The study analyzed normalized ultimate bearing capacity variations with soil strength parameters and foundation configurations. Increasing the cohesive strength of clay enhances the overall bearing capacity, which agrees with previous studies.
II. Traditional fixed-base assumptions underestimate the real structural behavior under vertical and lateral loads. Flexible soil foundations significantly alter the distribution of internal forces and displacements in structures.
III. Vertical loads are fully transferred to the foundation without deformation in the fixed-base case. In the SSI case, settlements occur, causing redistribution of forces and increased bending moments in columns.

© ASCE

IV. Under lateral loads, SSI increases the lateral drift of the structure. Foundation tilting occurs due to soil flexibility, reducing the stiffness and increasing the sway of the building. The fixed-base model underestimates lateral deformations, which are crucial for accurate seismic performance assessment.

V. The results highlight the necessity for advanced soil-structure interaction modeling in engineering practice. Geotechnical site investigations must be conducted before finalizing the foundation design for critical structures. Incorporating SSI effects in design reduces uncertainties and improves the resilience of structures under real-world conditions. Foundation flexibility must be incorporated in seismic design codes to improve the reliability of RC buildings in seismic-prone areas.

This study highlights the importance of considering Soil-Structure Interaction (SSI) in structural analysis to improve the accuracy of displacement predictions, stress distribution, and seismic performance assessments.

## REFERENCES

Abdulhahz, O., Al-Shenawy, A., and Awad, A. (2005). Derivation of Bearing Capacity Equation for a Two Layered System of Weak Clay Layer Overlaid by Dense Sand Layer. *Pertanika J. Sci. & Technol* 13, 213–235.

Bolisetti, C., and Whittaker, A. S. (2020). Numerical investigations of structure-soil-structure interaction in buildings. *Eng Struct* 215.

Chanda, D., Saha, R., Haldar, S., and Choudhury, D. (2023). State-of-the-art review on responses of combined piled raft foundation subjected to seismic loads using static and dynamic approaches, *Soil Dynamics and Earthquake Engineering*, Elsevier, 169, 107869.

Das, T., Baishya, R., Rakesh, K., Choudhury, D., and Rashid, H. (2025). Geotechnical challenges for high-rise buildings in Mumbai, India, In: *Proceedings of the Geotechnical Frontiers 2025. ASCE, Louisville, KY, USA, Geotechnical Special Publication No. GSP 364*, ISBN 978-0-7844-8597-2, pp. 94-103.

Das, T., Sharma, M., and Choudhury, D. (2023). Bearing Capacity and Liquefaction Assessment of Shallow Foundations Resting on Vibro-Stone Column Densified Soil in Vallur Oil Terminal, India. Indian Geotechnical Journal 53, 1392–1413.

Debnath, P., and Dutta, S. C. (2024). Seismic Retrofitting and strengthening of structures, in: *RC Structures Strengthened with FRP for Earthquake Resistance. Springer Nature Book Series*.

Debnath, P., and Dutta, S. C. (2023). In-plane and out-of-plane strength of different masonry bonds along with the effect of some waste materials for strengthening masonry wallets. *Journal of Building Engineering* 73.

Debnath, P., Dutta, S. C., Halder, L., and Choubey, B. (2023a). Lateral behaviour of unreinforced masonry walls with different sizes and locations of opening and effect of strengthening measures: a computational approach. *Bulletin of Earthquake Engineering.*

Debnath, P., Dutta, S. C., and Mandal, P. (2023b). Lateral behaviour of masonry walls with different types of brick bonds, aspect ratio and strengthening measures by polypropylene bands and wire mesh. *Structures* 49, 623–639.

Debnath, P., Halder, L., and Dutta, S. C. (2022). Damage survey and seismic vulnerability assessment of unreinforced masonry structures in low-intensity Ambasa earthquake of northeast India. *Structures* 44, 372–388.

© ASCE

Debnath, R., and Halder, L. (2019). A comparative study of the seismic provisions of Indian seismic code is 1893-2002 and draft Indian code is 1893:2016, in: *Lecture Notes in Civil Engineering*. Springer, pp. 151–160.

Dutta, R. K., and Rao, G. V. (2008). *Potential of Coir Based Products as Soil Reinforcement, International Journal of Earth Sciences and Engineering*.

Eurocode 8. (2004). *English version Eurocode 8: Design of structures for earthquake resistance-Part 1: General rules, seismic actions and rules for buildings*.

Fatahi, B., Basack, S., Ryan, P., Zhou, W. H., and Khabbaz, H. (2014). Performance of laterally loaded piles considering soil and interface parameters. *Geomechanics and Engineering* 7, 495–524.

Fatahi, B., and Tabatabaiefar, S. H. R. (2024). Effects of Soil Plasticity on Seismic Performance of Mid-Rise Building Frames Resting on Soft Soils. *Advances in Structural Engineering* 17.

Gupta, A., Dutta, R. K., Shrivastava, R., and Khatri, V. N. (2017). Ultimate Bearing Capacity of Square/Rectangular Footing on Layered Soil. *Indian Geotechnical Journal.* 47, 303–313.

Halder, L., Dutta, S. C., Debnath, P., and Sharma, R. P. (2021). Seismic vulnerability assessment of low-rise unreinforced masonry buildings in Northeast India considering variability of material properties. *Asian Journal of Civil Engineering* 22, 843–863.

Hamidia, M., Shokrollahi, N., and Nasrolahi, M. (2021). Soil-structure interaction effects on the seismic collapse capacity of steel moment-resisting frame buildings. *Structures* 32, 1331–1345.

Hokmabadi, A. S., Fatahi, B., and Samali, B. (2014). Assessment of soil-pile-structure interaction influencing seismic response of mid-rise buildings sitting on floating pile foundations. *Comput Geotech* 55, 172–186.

IS 19117. (2025). *Design and Construction of Combined Piled Raft Foundations – Code of Practice, Bureau of Indian Standard (BIS)*, Manak Bhavan, New Delhi, India.

Katzenbach, R., Leppla, S., and Choudhury, D. (2016). Foundation Systems for High-Rise Structures, published by CRC Press, Taylor & Francis Group, USA and UK, ISBN: 978-1-4987-4477-5, pp. 1-298.

Kulkarni, S. K., Shiyekar, M. R., Shiyekar, S. M., and Wagh, B. (2014). Elastic properties of RCC under flexural loading-experimental and analytical approach. *Sadhana* 39, 677–697.

Lamb, H. (1904). On the Propagation o f Tremors over Surface o f an Elastic S, in: *Proceedings of The Royal Society of London*. Royal Society.

Patil, G., Choudhury, D., and Mondal, A. (2023). Interactive iterative methodology for seismic analysis of pile-raft supported nuclear power plant structure in a conventional framework, *Soil Dynamics and Earthquake Engineering*, Elsevier, 173, 108109.

Raj, D., Singh, Y., and Kaynia, A. M. (2024). Seismic fragility analysis of coupled building-slope systems. *Earthq Eng Struct Dyn* 53, 116–137.

Ravi Kiran, N., Singh, Y., and Jakka, R. S. (2023). Biaxial capacity envelopes for the capacity design of biaxially loaded shallow foundations. *Soil Dynamics and Earthquake Engineering* 175.

Reissner, E. (1936). Stationäre, axialsymmetrische, durch eine schüttelnde Masse erregte Schwingungen eines homogenen elastischen Halbraumes. *Ingenieur*-Archiv 7, 381–396.

Sáez, E., Lopez-Caballero, F., and Modaressi-Farahmand-Razavi, A. (2011). Effect of the inelastic dynamic soil-structure interaction on the seismic vulnerability assessment. *Structural Safety* 33, 51–63.

**© ASCE**

Saha, R., Dutta, S. C., Haldar, S., and Kumar, S. (2020). Effect of soil-pile raft-structure interaction on elastic and inelastic seismic behaviour. *Structures* 26, 378–395.
Tahghighi, H., and Mohammadi, A. (2020). Numerical Evaluation of Soil–Structure Interaction Effects on the Seismic Performance and Vulnerability of Reinforced Concrete Buildings. *International Journal of Geomechanics* 20.
Wolf. (1985). *Dynamic Soil-Structure Interaction*. Prentice-Hall.

© ASCE